Computers and Geotechnics 97 (2018) 167–188

Contents lists available at ScienceDirect

Computers and Geotechnics

journal homepage: www.elsevier.com/locate/compgeo

Research Paper

On the micro mechanics of yielding and hardening of crushable granular soils

John P. de Bono*, Glenn R. McDowell

University of Nottingham, United Kingdom

ARTICLE INFO

Keywords:
Discrete element method
DEM
Sand
Yielding
Yield surface

ABSTRACT

Stress path tests are used to investigate the yield surface of a crushable numerical soil. Triaxial samples with isotropic and anisotropic stress histories are examined to determine the nature of the yield surface and to establish what governs yield. Two separate yield surfaces are exposed: a shear yield surface at low p' and high η which is governed by minor breakage of fine particles, and a compressive yield surface at high p' and low η, governed by bulk breakage across all particle sizes. The shear yield surface is dependent on stress history, whilst the compressive yield surface is isotropic.

1. Introduction

It has recently been shown that it is possible to reproduce a wide range of aspects of soil behaviour using the discrete element method (DEM). With a simple crushing model and real particle strengths, the authors have produced realistic normal compression lines, whilst also resulting in the correct fractal particle size distribution when compared to experimental data [1,2].

Following this, the same crushing model was used to explore triaxial shearing and critical states, and a realistic critical state line was obtained, parallel to the NCL in log e–log p' space at high stresses [3]. A range of constant-σ_3, constant-p', and constant-volume triaxial tests were performed, resulting in realistic stress-dilatancy plots, and by normalising the stress states by the apparent pre-consolidation pressure, a state boundary surface was established.

It is the intention here to take a closer look at yielding and to establish the yield surface of this numerical soil as a function of stress history. This will begin first by briefly mapping out the yield surface(s) using a suitable definition of yield from the macroscopic stress-strain responses. Then focus will be given to the micro scale behaviour and underlying mechanisms that result in yield at various combinations of stresses, as well as analysing the effects of anisotropy and stress-history on the yield surface.

2. Model background

The results presented here are all obtained from simulations using the DEM software PFC [4], using spheres to model sand. The crushing model used is identical to that used previously [1,5], and uses the average octahedral shear stress in the particles to determine whether or not a particle breaks:

$$q = \frac{1}{3}[(\sigma_1-\sigma_2)^2 + (\sigma_2-\sigma_3)^2 + (\sigma_1-\sigma_3)^2]^{1/2} \quad (1)$$

where $\sigma_{1,2,3}$ are the average principal stresses in the particle, caused by and calculated from contacts with neighbouring bodies. When a particle is in a state of incipient breakage, it is replaced by two smaller spherical fragments positioned within the former boundary of the 'parent' particle. Conservation of mass is obeyed, which means that the fragments overlap (this overlap requires a number of timesteps to be completed immediately following breakage to allow energy dissipation). For full details of the crushing mechanism, readers are referred to the original publication [1], which includes an investigation of the number of fragments, and to slightly more recent work [5] which compares a range of breakage criteria. The particles strengths are attributed according to a hardening law of the form:

$$q_0 \propto d^{-b} \quad (2)$$

where q_0 is a representative strength and the parameter b represents the size-effect on particle strength. The strengths used were obtained experimentally from a silica sand [6]. The strength q_0 is a value such that 37% of particles of that size are stronger, and, together with a Weibull modulus m, is used to describe a Weibull distribution of strengths. For the silica sand, the q_0 value for 2 mm particles is 37.5 MPa, and the Weibull modulus for the silica sand is 3.3. The q_0 values for other sizes of particle is calculated according to Eq. (2), where $b = (3/3.3) \approx 1$. Individual particle strengths for any given size are distributed according to a Weibull distribution using the q_0 value and $m = 3.3$.

* Corresponding author.
E-mail address: john.debono@nottingham.ac.uk (J.P. de Bono).

https://doi.org/10.1016/j.compgeo.2018.01.010
Received 26 September 2017; Received in revised form 11 December 2017; Accepted 17 January 2018

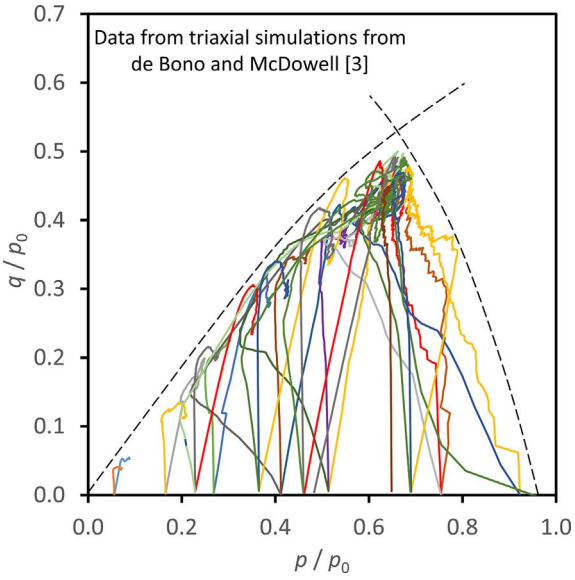

Fig. 1. State boundary surface obtained from triaxial tests.

Using these strengths and hardening law, the authors recently performed a series of constant-σ_3, constant-p' and constant-volume triaxial test simulations on samples with a range of stress histories [3]. These resulted in a realistic critical state line which was parallel to the NCL at high stresses and non-unique at low stresses for compacted or over-consolidated samples, in agreement with experimental data for sand [7]. By normalising the stress states during the triaxial tests by the apparent pre-consolidation pressure a unique state boundary surface was obtained, which is shown in Fig. 1. The shape of this state boundary surface agreed well with experimental data for sand [8], and suggests two distinct mechanisms of yielding (as opposed to a single elliptical yield surface), as suggested by authors such as Chandler [9] and Wood [10].

To examine the yielding and establish yield surfaces for this sand, a comprehensive series of stress-path tests are now simulated, covering all directions in q–p' space on triaxial samples with a range of stress-histories. The stress-paths performed on each sample are shown schematically in Fig. 2(a). Similar 'rosettes' of stress-paths tests were performed experimentally by Yasufuku et al. [11] and Smith et al. [12], and numerically using DEM by Cheng et al. [13], albeit with agglomerates.

The triaxial samples are enclosed vertically by 2 rigid platens and laterally by a flexible, faceted cylindrical membrane, an example image of which is given in Fig. 2(b), and described in more detail in [3]. The samples on which the stress-path tests are performed are all derived from an initially mono-disperse sample, 30 mm in height and 15 mm in diameter, consisting of 723 particles of 2 mm diameter. This sample is subjected to compression to various stresses and crushing before any stress-path tests to create more realistic graded samples with a much larger number of particles.

The simulations are stress-controlled, using stress-path increments of 25 kPa ($=\sqrt{(\delta q^2 + \delta p^2)}$). Stresses are applied to the samples via both the platens and membrane using servo-controls, and each simulation is terminated when $|\delta\varepsilon_1| \geq 0.5\%$.

3. Experimental yielding of granular soil

Yielding is understood to be the transition from elastic to plastic behaviour. For soils, this is usually interpreted as a clear change in the stress-strain response, whereby the behaviour changes from a stiff to a less-stiff regime. Soils do not in general show a discontinuous stress-strain response, like an ideal elastic-plastic material. Any truly-linear elastic behaviour typically only spans very small strains, e.g. < 0.001% [14], and significant changes in stiffness may occur relatively gradually, making identification of a yield point less obvious. As such, there are a variety of methods typically used for identifying the yield point—e.g. the end of linear behaviour, the point of intersection between two fitted lines, the point of maximum curvature, or simply taking an intuitive judgement 'by eye', which is, of course, rather unscientific.

Experimentally, one of the prominent earlier studies on the yielding of sand is that by Poorooshasb et al. [15], who performed multiple stress-path tests using the triaxial apparatus to establish enough yield points to construct a yield surface. A feature of their tests was that each yield point was reached through increasing the stress ratio η (at relatively moderate stress levels for a silica sand), and so their established yield surface was 'open' along the p-axis in q-p' space, and did not

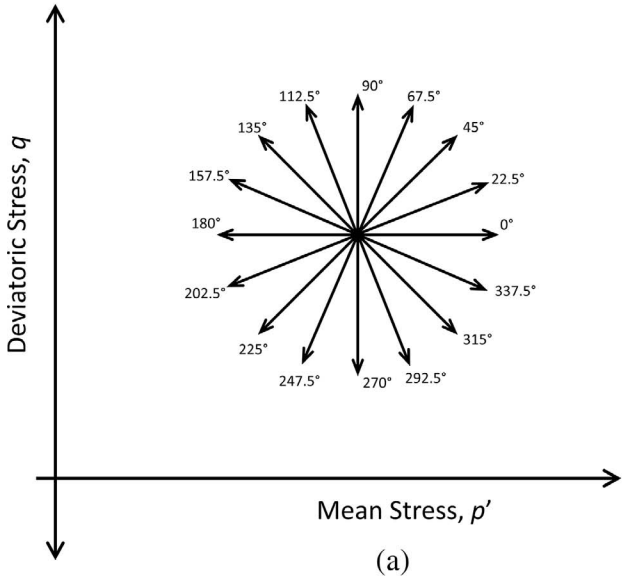

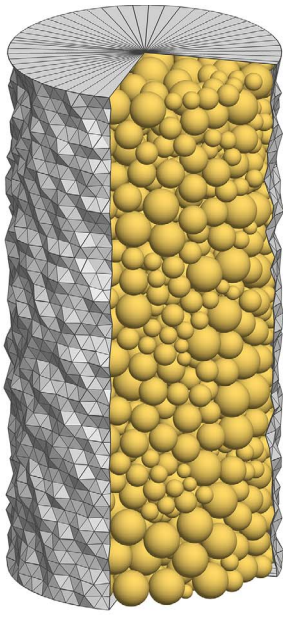

Fig. 2. Stress-paths (a) and image of typical triaxial boundaries and sample (b).

consider the yielding that occurs during isotropic compression. They identified yielding using a method similar to the Casagrande method (two fitted lines), from plots of shear stress against axial strain. It was found that yielding occurred at an approximately constant stress ratio.

Tatsuoka and Ishihara [16] conducted similar tests using elaborate stress-paths, identifying yield points from a combination of shear and volumetric stress-strain plots, as the points at which 'appreciable strains' commence. The yield surfaces they established were slightly more curved than Poorooshasb et al. [15], but were also open along the p-axis. It was noted that at relatively lower stresses the yield surfaces were approximately linear in q–p' space. Ishihara et al. [17] and Vermeer [18] subsequently showed that lines of constant shear strain ε_q, when plotted in q–p' space were very similar in shape to the yield surfaces. Researchers such as Vermeer [18] and Lade [19] proposed closing such yield surfaces by combining with an additional compressive yield surface along the p-axis. Chandler [9] also encouraged the use of 2 separate envelopes to construct the yield surface for granular materials, based on the theory of envelopes and some assumptions about dissipation functions.

Miura et al. [20] and Yasufuku et al. [11] established enclosed yield surfaces from series of stress-paths tests on sands. Miura et al. [20] identified yield points as the points of maximum curvature from q–ε_q and p–ε_v plots, whilst Yasufuku et al. [11] used plots of η against various measures of strain, using the intersection of 2 straight lines. The yield surfaces obtained in both cases were elliptical in form. Yasufuku et al. [11] focused on investigating the shape of yield surfaces for anisotropic sands, and their results indicated that their shape or orientation were highly-dependent on previous loading paths.

Authors including Jardine et al.[12,21–23] meanwhile presented experimental results on a range of materials including sand supporting the concept of kinematic yield surfaces [24]. Kinematic yield surfaces, in general, are inner, translating yield surfaces, enclosed within an outer yield or bounding surface. In their results, the inner yield surfaces were generally linked to various stages of degradation of some measure of tangent stiffness, whilst the outermost surface was generally taken as when soil stiffness had reduced completely and large strains commenced. This approach can satisfactorily explain the observed anisotropy in soil responses.

In addition to the above examples of experimental work on yield surfaces, there are innumerable theoretical and analytical descriptions of yield surfaces for soils available in the literature. Such models vary in complexity, and may consist of one or more surfaces in q–p' space, which may include rotational hardening and kinematic hardening in addition to volumetric hardening.

This paper therefore uses a previously validated DEM crushing model to established what governs 'yield' for the 'numerical soil'. References are made to experimental work of others, but the focus here is to examine the micro mechanics of what is observed in the DEM model, provided that the model gives macroscopic responses in agreement with previously published data.

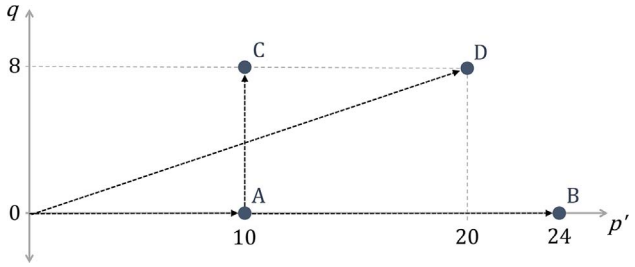

Fig. 3. Schematic showing stress states prior to various stress-path series.

4. Simulation results

This section contains the results and ordered discussion of 5 sets of stress-path tests. Table 1 and Fig. 3 provide a summary of the initial samples used in each case.

4.1. Simple yielding of a compacted sand

The most basic set of simulations were performed on a triaxial sample isotropically compressed to $p' = 10$ MPa. This sample is referred to as 'compacted', to emphasise that it is not yet on the plastic normal compression line (i.e. is on a virgin loading line in e–p' space). From this compacted state, the 16 stress-path tests (Fig. 2a) were then performed. This particular sample is shown in Fig. 2(b), and consists of 2030 particles (further details are given in Table 1).

The two fundamental stress-strain plots in terms of axial and radial components are shown for the 16 tests in Fig. 4. The simulations loaded with small (or no) deviatoric component δq (e.g. 0°, 22.5°…) display approximately linear initial behaviour, before both the axial and radial tangent stiffnesses (i.e. the gradient) decrease abruptly, a clear indication of yield. For most of the other simulations (e.g. 90°), the axial and radial tangent stiffnesses decrease more gradually with strain, making precise determination of the yield point less clear. Additionally, for some of simulations (e.g. 157.5°), either the axial or radial stiffness does not decrease monotonically—making physical interpretation of a yield point difficult.

It is necessary to have a rigorous definition of yield which can be applied to all simulations. Interpreting yielding as being associated with a decrease in stiffness, and the onset of greater strains, a simple such definition could therefore be when the tangent stiffness decreases by a certain factor [23]. Such an example is given in Fig. 5, which plots the yield points defined as when the tangent stiffness drops to $\leq 50\%$ of its initial value, from both the axial and radial stress-strain data. Only 7 of the simulations enable yield points to be estimated from both axial and radial responses, which do not always coincide. One response to this disparity could be to take an average from the two yield points [16]; Wood [10] for example suggests using as many different plots of stress and strain variables as reasonably possible to confidently identify yield points.

Using a different approach, Tavenas et al. [25] plotted the cumulative work (or strain energy) against mean stress p' to identify yield

Table 1
Details of initial samples for each test series.

Sample name/description	Current stress (MPa)		Max. prev. stress (MPa)		No. particles:	Voids ratio, e	Particle size (mm):		Loading history (Fig. 3)
	p'	q	p'	q			d_{50}[a]	d_{min}	
Compacted	10	0	10	0	2030	0.62	1.45	0.5	0A
Overconsolidated	10	0	24	0	5551	0.56	1.26	0.2	0BA
Deviatoric	10	0	10	8	2154	0.61	1.45	0.4	0ACA
Isotropic NC	24	0	24	0	5551	0.53	1.26	0.2	0B
Anisotropic NC	20	8	20	8	6004	0.54	1.23	0.16	0D

[a] d_{50} obtained from conventional PSD plot of % by mass passing versus particle diameter (actual median particle size is smaller).

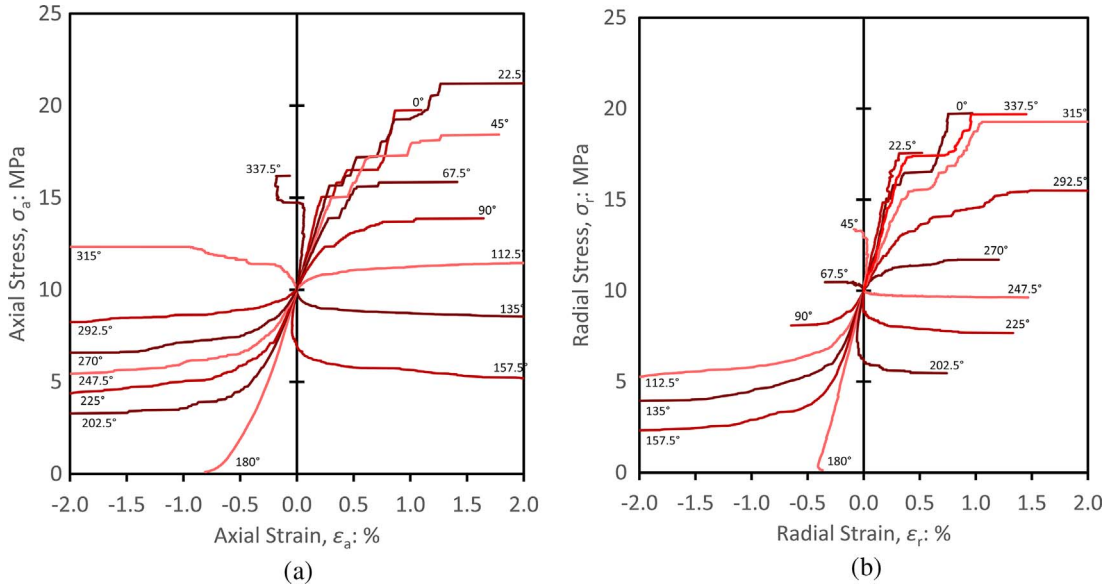

Fig. 4. Axial (a) and radial (b) stress-strain plots.

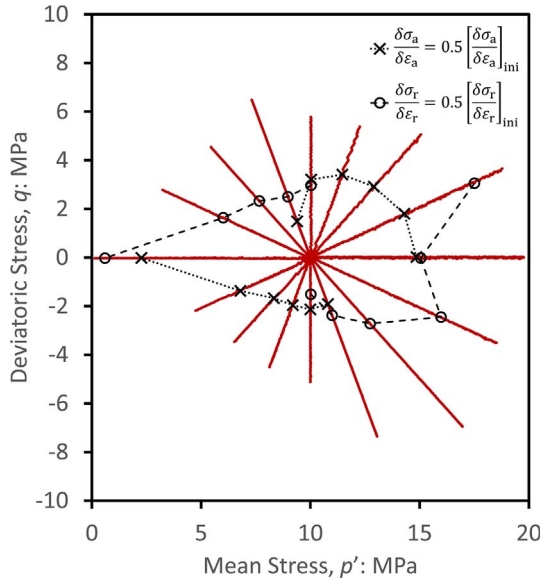

Fig. 5. Yield points derived from axial and radial tangent stiffnesses.

from a single pair of variables for a similar series of stress-path tests on one-dimensionally normally consolidated clay. Graham et al. [26] later used plots of cumulative work against the length of stress-path (in terms of q–p') to identify yield, thereby incorporating all components of stress and strain increments, enabling a single plot to be used for any stress-path. The data from Tavenas et al. [25] is reproduced in Fig. 6(a), alongside an equivalent plot for the DEM simulations in (b). The trends in both plots are similar, despite the difference in stress level. Plotting the data from the simulations in this manner does not necessarily make yield points any more well-defined; there is still uncertainty due to the simulations displaying a combination of rapid and gradual yielding. The cumulative work does not increase monotonically in all stress-paths—in both the experimental and numerical results, stress-paths in which $\delta p' < 0$ show an initial decrease in W.

Nonetheless, taking yield as the point at which the incremental work resulting from a single stress increment is greater than an arbitrary threshold of 2 kJ/m^3 results in the yield points shown by the crosses in Fig. 6(b). These enable a yield surface shown in Fig. 7(a) to be constructed. Fig. 7(b) shows comparable data for a sand from Yasufuku et al. [11], also obtained from plots of cumulative work. The two yield surfaces are broadly similar: both are elliptical in shape, and in comparison to anisotropically-prepared samples (shown later), are relatively isotropic in shape (the experimental yield surface displays more prominent anisotropy, most likely due to the method of sample preparation).

The deviatoric and volumetric responses are shown for the same set of simulations in Fig. 8. The deviatoric shear responses (a) appear more consistent than the axial or radial data in the sense that changes in shear stress q are accompanied by corresponding shear strains of the same sign. The tangent measured from such a plot is proportional to the shear modulus G, and the results suggest a constant initial value, G_{ini} at very small strains. Some simulations display a sudden decrease in stiffness whilst others display a gradual decrease beginning almost immediately. All simulations display the same overall trend, with G_{tan} decreasing from the initial value G_{ini} as yielding occurs.

The volumetric behaviour is shown in Fig. 8(b), and in this plot the tangent gradient is interpreted as the bulk modulus K. The data suggest a constant initial modulus, K_{ini}, independent of stress path. For the simulations with increasing mean stress ($\delta p' > 0$), the initial response is approximately linear before a clear change in behaviour, i.e. K_{tan} remains fairly constant until abruptly decreasing, clearly indicating yield. Of these, the simulations with relatively small increments of shear stress δq (e.g. 0°, 22.5°…) reach the highest values of mean stress before yielding, which is consistently associated with the onset of particle crushing.

For the $\delta p' < 0$ simulations, the initial response is also linear, but in most cases (e.g. 112.5°) there follows an apparent increase in tangent stiffness as the sample exhibits contractive tendencies despite p' reducing. The point at which this non-linearity occurs and K_{tan} appears to increase invariably coincides with the shear stiffness G_{tan} rapidly degrading. Hence it would appear that these are plastic volume changes related to the dilatancy, which occur simultaneously with a loss of shear strength. Closer inspection reveals that these transient contractive tendencies often coincide with minor particle breakage. Although p' is decreasing, the increasing magnitude of deviatoric stress is enough to cause a small degree of particle breakage, which facilitates a certain amount of rearrangement and densification. This phenomenon is followed by a more dramatic loss in stiffness later. With the exception of the 292.5° simulation, the trend is the same for all simulations whereby changes in p' are accompanied by volumetric strain of the same sign, yielding (ultimately) resulting in a loss of stiffness.

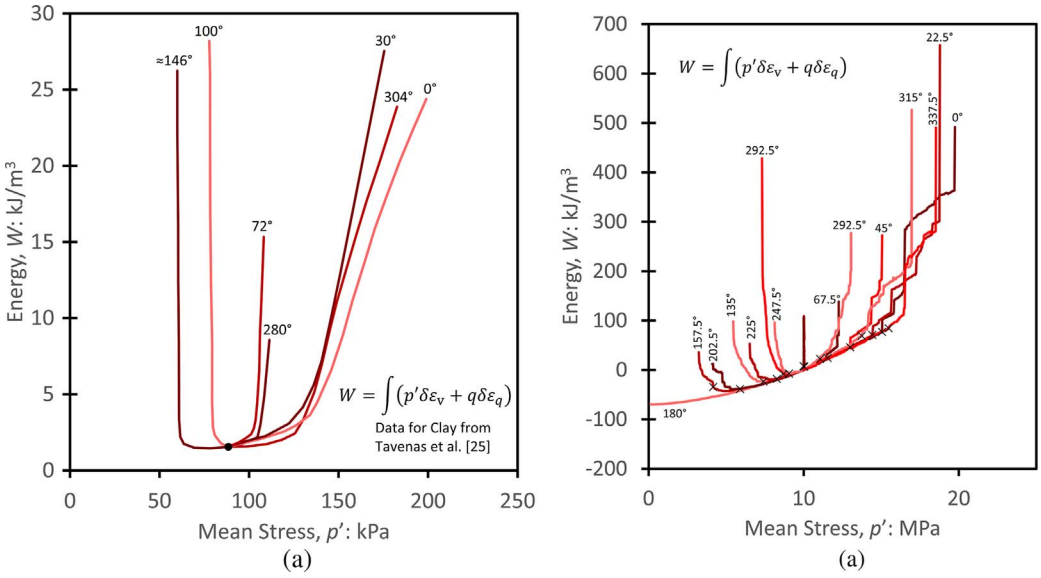

Fig. 6. Cumulative work versus mean stress: experimental data (a) and DEM data (b).

Using the same crude approach as above (defining yield as the point at which the tangent stiffness decreases to < 50% of the initial value) leads to the yield points/surfaces in Fig. 9(a) from the deviatoric and volumetric responses. For this purpose, some conditions were necessary in calculating the tangent stiffness (gradient), for ease of interpretation. Due to the very small stress increments applied, the gradient calculated between any two neighbouring points was subject to large variations. It was therefore planned to use a linear regression-type method to calculate the best-fit gradient across a range of neighbouring data points (e.g. Jovičić and Coop [27]), however this did not always capture the exact point of yielding. Instead, for any single data point, the current tangent is taken as the maximum gradient found between this current point and any future subsequent data points (within a certain range of stress increment, typically 500 kPa). An additional condition was that the tangent was not allowed to increase, and only decrease. This method avoids large fluctuations of stiffness, and specifically avoids giving the impression of a complete loss of stiffness due to a singular, momentary low gradient between two neighbouring points. For example, for the 67.5° simulation, this is the case in the q-ε_q curve at around 0.25% strain. Calculating the tangent stiffness in the above way produced stiffness-strain plots which visually corresponded well with all of the presented data.

Comparing the yield surfaces in Fig. 9 shows that for the simulations that yield at relatively lower p', degradation of the bulk modulus occurs at higher stress ratios (i.e. later) compared to the shear modulus. Simulations that yield at relatively higher p' show degradation occurs approximately simultaneously. The state-paths are shown in e–p' space in Fig. 9. In the inset, the results of two simulations are highlighted showing the yield points defined according to G_{tan} and K_{tan}. For the 45° simulation, yielding according to both G_{tan} and K_{tan} occurs at approximately the same point, whereas for the 225° simulation, loss of bulk stiffness occurs much later than the shear stiffness.

Although using different methods of defining yield, Tavenas et al. [25] and Yasufuku et al. [11] both observed and commented on similar disparities between yield points obtained from different measured variables; Tavenas et al. [25] in particular noted that the p'–ε_v responses were unsuitable for observing yield clearly in the 90–270° ($\delta p' < 0$) range.

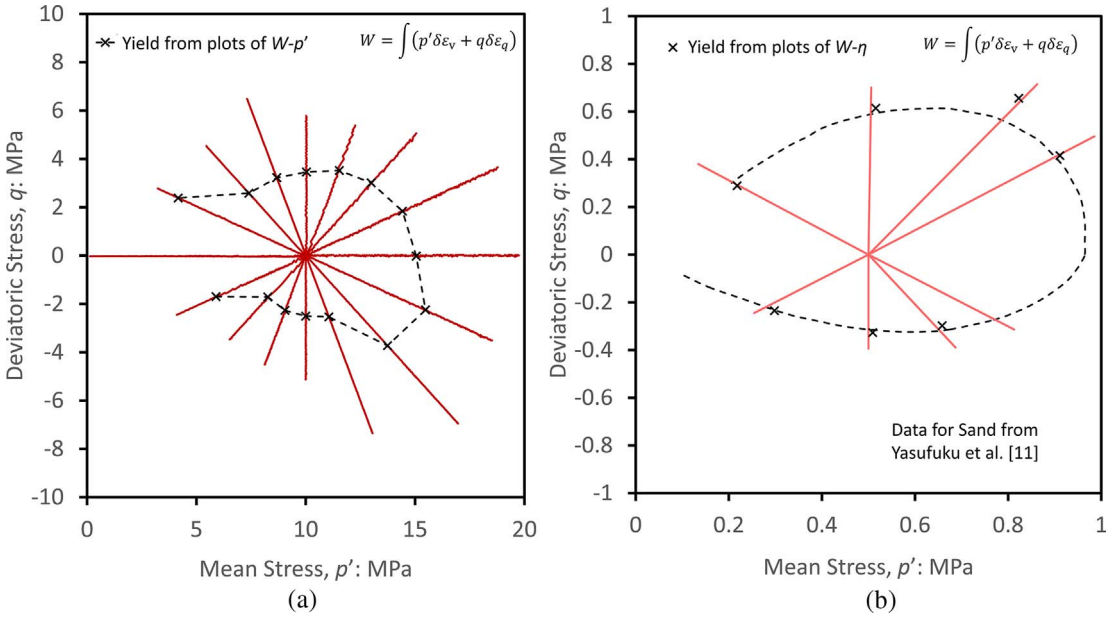

Fig. 7. Yield surfaces derived from cumulative work: DEM results (a) and experimental data (b).

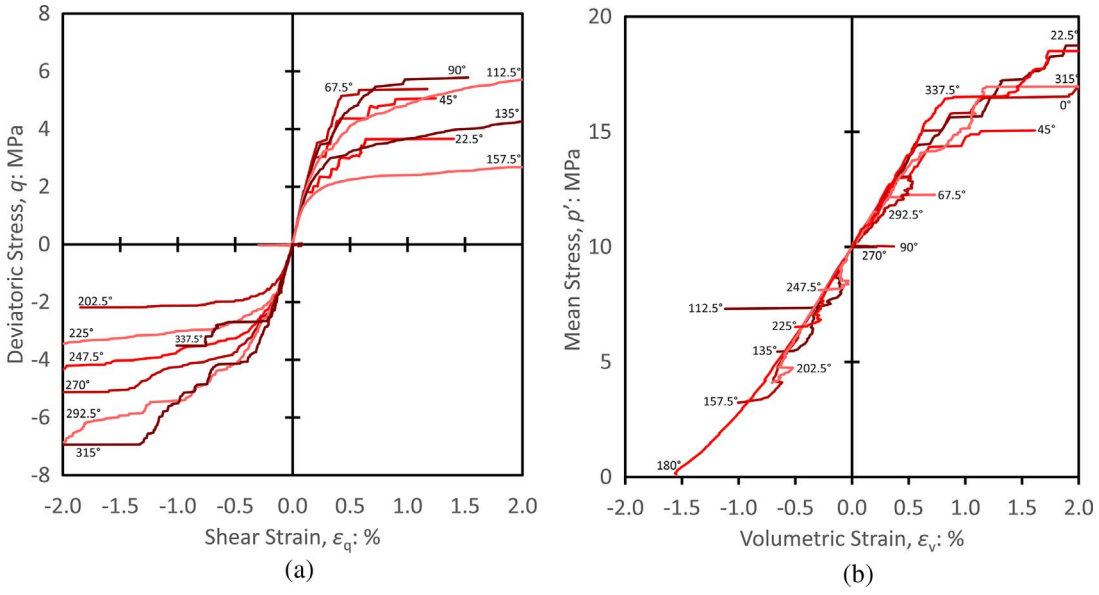

Fig. 8. Deviatoric (a) and volumetric (b) stress-strain responses.

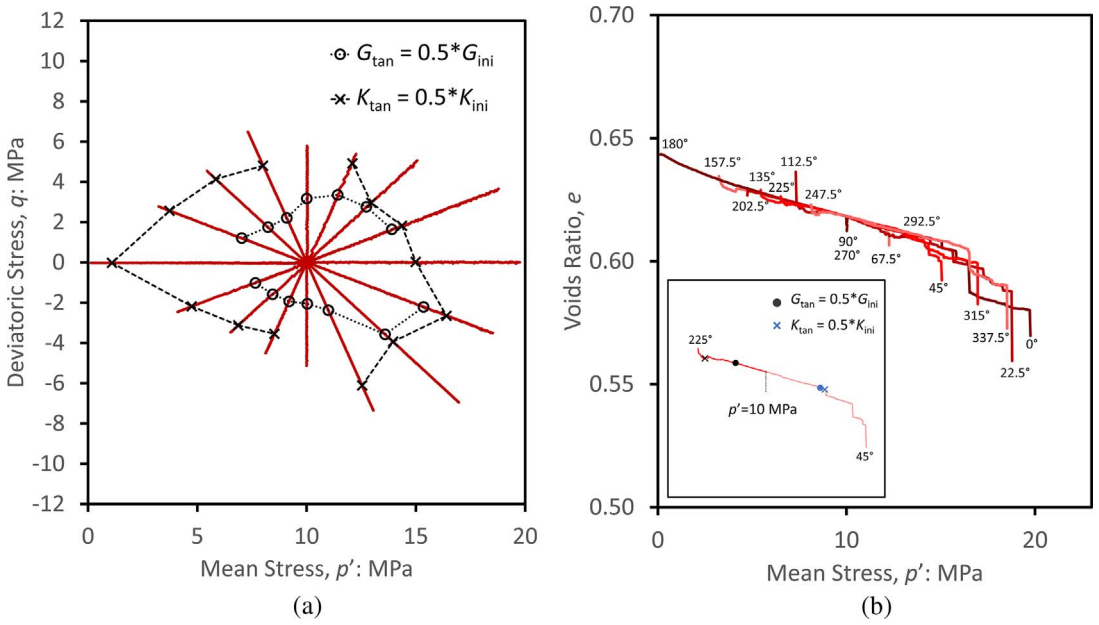

Fig. 9. Yield points from deviatoric and volumetric responses (a), and state paths in e–p' space (b).

Broadly speaking, the trend shown in Fig. 9(b) is observed across all tests, i.e. for stress-paths which reach high p', loss of stiffness occurs rapidly whereby both G_{tan} and K_{tan} reduce from their initial values to minimal values together and instantaneously; whilst for stress-paths which yield at low p', G_{tan} decreases gradually whilst K_{tan} either remains steady or increases, and then degrades once G_{tan} has reached a minimal value. The ratio of G_{tan}/K_{tan} decreasing implies that there are finite contacts remaining, but sliding, rolling, abrasion or damage to small particles is occurring—this will be examined later.

It is well accepted that for sands, there are two separate types of yielding [9,10]—one in which the main cause of permanent deformation/rearrangement is caused by the mobilised friction (shearing), the other in which the dominant cause of permanent deformation appears to be particle crushing caused by high mean stress. The results shown thus far would support this—there are two distinct modes of stiffness degradation depending on the stress level.

In order to further clarify and differentiate between these two distinct modes of yielding, as well as to confidently identify when yielding occurs (avoiding use of arbitrary thresholds), what occurs at the micro-scale during the stress-path tests will now be investigated. To achieve this, an overconsolidated sample will now be analysed with separate attention given to yielding at low and high stresses, for which the preconsolidation pressure is known, and therefore the onset of plastic strains in isotropic compression should be clearly defined. Subsequent sets of simulations will then later be presented investigating further the effects of stress-history and determining whether the *shape* of the yield surface is constant.

4.2. Detailed yielding of overconsolidated sand

4.2.1. Shear yielding under increasing $|\eta|$

The following set of results are obtained from an initial sample that has first been isotropically compressed to 24 MPa—well on to the normal compression line—then unloaded isotropically to $p' = 10$ MPa.

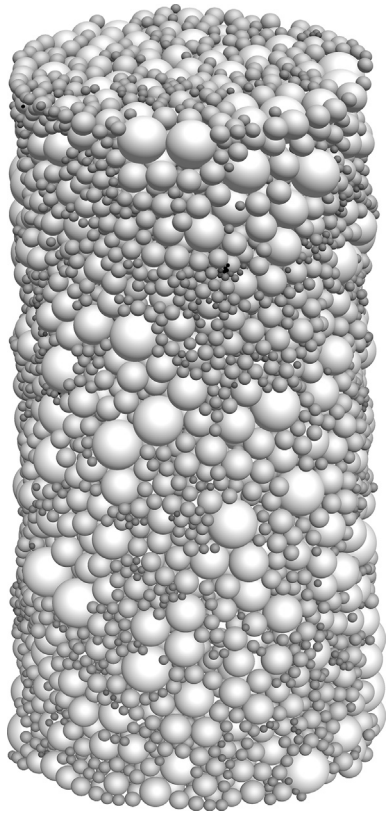

Fig. 10. Crushed overconsolidated sample, darker shading indicates smaller particle size.

In comparison to the previous compacted sample, this overconsolidated sample is denser (Table 1) and has undergone more extensive crushing, providing a broader PSD, which is shown in Fig. 10. To investigate the shear yielding, i.e. yielding which occurs at relatively low mean stresses and at relatively large magnitudes of stress ratio, attention will firstly be given to the deviatoric shear stress responses.

Fig. 11(a) shows the deviatoric responses, and these suggest an approximately single initial shear modulus, G_{ini}, for all tests ($\approx$500 MPa). For most of the responses there is a gradual degradation of modulus (G_{tan}), the clearest exceptions being the 22.5° and 337.5° simulations. These two tests yield at the highest p' and G_{tan} remains almost constant before sudden yielding. In the 157.5° and 202.5° simulations by contrast, G_{tan} decreases more gradually and almost immediately upon loading.

The responses in terms of stress ratio are given in Fig. 11(b). Most tests collapse onto a single η–ε_q curve, showing an 'intrinsic' relation between stress ratio and shear strain. This shows that for these tests, the onset and accumulation of shear strain and therefore yielding is a function of stress ratio. This is consistent with many of the experimental observations discussed earlier [15,17], in which the yield surfaces corresponded to lines of constant η and/or with contours of constant shear strain. It is much clearer in Fig. 11(b) that the 22.5°, 45°, 67.5°, and 337.5°, 315° simulations display different behaviour, showing a loss of shear strength at smaller shear strains. These follow the same behaviour as all other tests until appearing to yield and diverging from the intrinsic η–ε_q curve. These tests are those that yield at the largest p'. The behaviour appears a function of stress ratio or mobilised friction until a great enough stress is reached in which case the behaviour is superseded by compressive yielding, illustrating the interplay between the two separate types of yielding [9,18].

Vermeer [18] suggested that shear yield surfaces are well-represented by contours of constant shear strain. Fig. 12 shows contours of constant shear strain for these simulations, which are directed from the origin at low stresses, whilst at high stresses larger shear strains occur at smaller stress ratios. For comparison, similar experimental data (but over a smaller stress range) for sand from Ishihara et al. [17] is shown in (b). The same linearity can be observed, with less curvature with increasing p' in the experimental data due to the lower stress levels and therefore less substantial crushing. Fig. 12(a) suggests that for this isotropic sample, deformation/yielding at low stresses is a function of stress ratio, whilst at higher stresses clearly another mechanism—particle breakage—begins to dominate.

4.2.2. Compressive yielding under increasing p'

The volumetric stress-strain behaviour for the overconsolidated sample is shown in Fig. 13(a). Again, there appears a single K_{ini}, independent of stress path. What is slightly clearer in comparison to the compacted sample, is that for this denser, more well-graded sand the pre-yield behaviour is not perfectly linear. Rather, K_{tan} approximately follows $K \propto p^{(1/3)}$, as would be predicted from purely Hertzian elasticity [28] which is the contact model used here. For sands, the pressure-dependency typically observed is often around $K \propto p^{(1/2)}$ [27,29]. In comparison to the compacted sample, there is no contractive behaviour

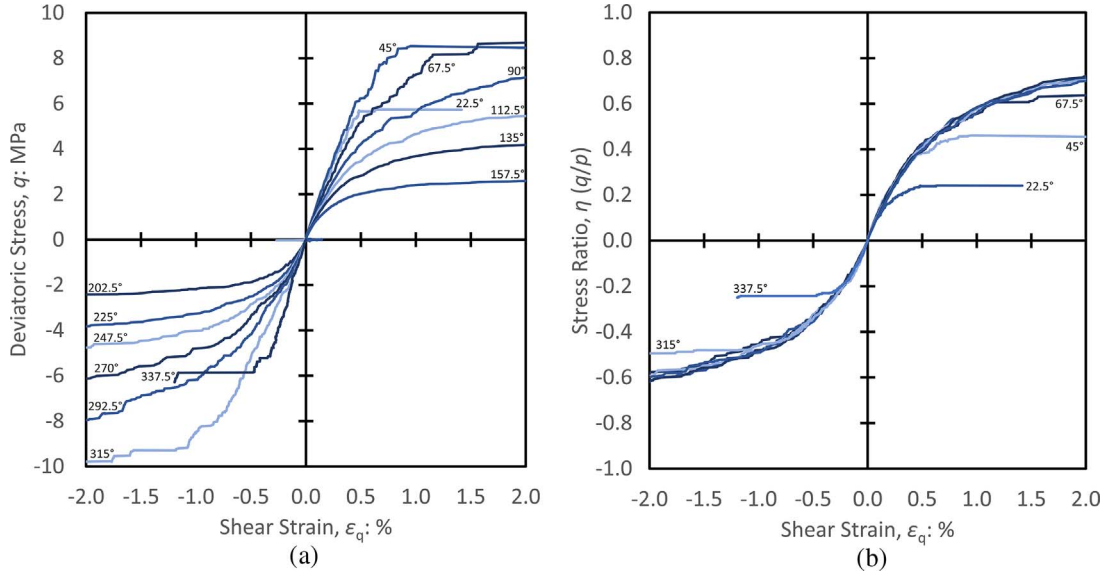

Fig. 11. Deviatoric (a) and stress ratio (b) responses for the overconsolidated sample.

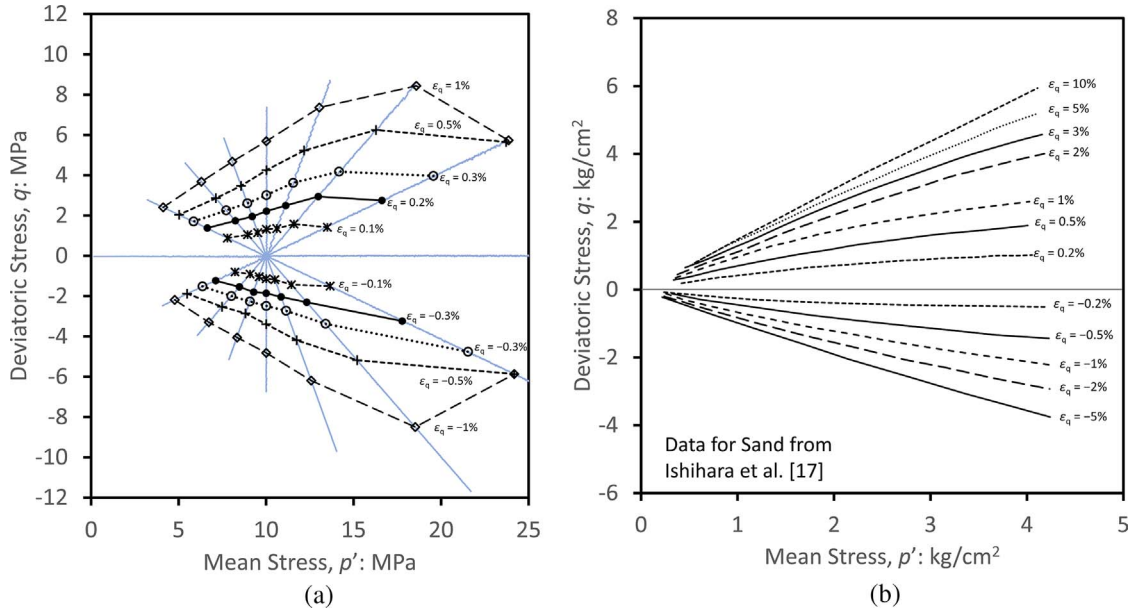

Fig. 12. Contours of shear strain: DEM data (a), typical experimental data (b).

evident in the simulations with $\delta p' < 0$, due to the initial sample being relatively denser, and the particles effectively stronger due to prior compression to a much greater stress.

For those tests which reach high mean stresses, compressive yielding again occurs suddenly, this sudden decrease in tangent bulk stiffness caused by the onset of large scale particle crushing (which will be shown quantitatively shortly). In comparison, for those tests in which p' reduces, K_{tan} reduces more gradually, and apparently due to shear yielding caused by increasing $|\eta|$. This is represented in Fig. 13(b), which shows how K_{tan} degrades with stress ratio for the $\delta p' < 0$ simulations. In these tests, K_{tan} decreases uniformly with $|\eta|$ (and therefore ε_q), reaching minimal values at approximately the same point. Minimal crushing occurs in these simulations, and the uniform rate of degradation of K_{tan} shows that the loss of bulk stiffness is a by-product of the sample undergoing shear yielding.

Measures of cumulative energy are often used as hardening parameters in soil models, and authors such as Tavenas et al. [25], Kuwano and Jardine [21] and Yasufuku et al. [11] all presented contours of energy in q–p' space. Yasufuku et al. [11] in particular gave plots of 'normalised strain energy' contours obtained from stress-path tests on an isotropically overconsolidated sand, which is reproduced in Fig. 14(a). Their results suggested that these contours gave reasonable representations of the yield surface. An equivalent plot for the over-consolidated simulations is given in Fig. 14(b) for comparison. The form of the contours are similar in both cases (isotropic and elliptical).

4.2.3. Particle crushing

Assuming that (compressive) yielding at relatively high p' is caused by crushing, it is necessary to quantify the amount and cause of particle breakage. Fig. 15(a) shows contours of particle breakage in terms of constant particle surface area, which provide an indication of how much crushing occurs. The contours are plotted in terms of % increase of surface area due to the very small numbers. The contours appear rounded and symmetrical about the p-axis. The first thing to note from these plots is that breakage occurs in nearly all simulations, even those that yield at relatively low p'; however it is clear a much greater degree

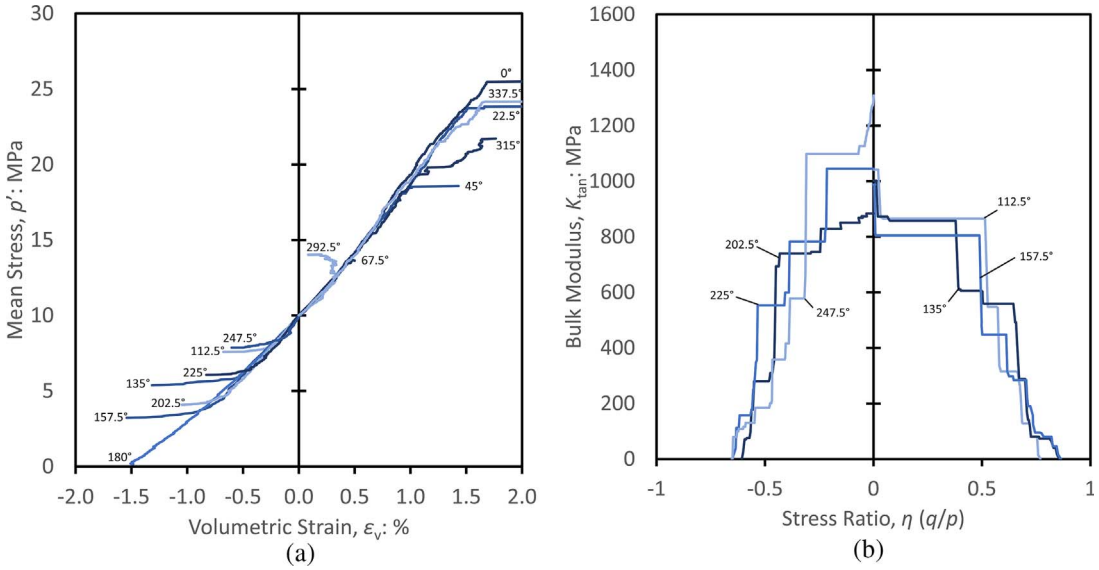

Fig. 13. Volumetric responses for OC simulations (a) and tangent bulk moduli against stress ratio (b).

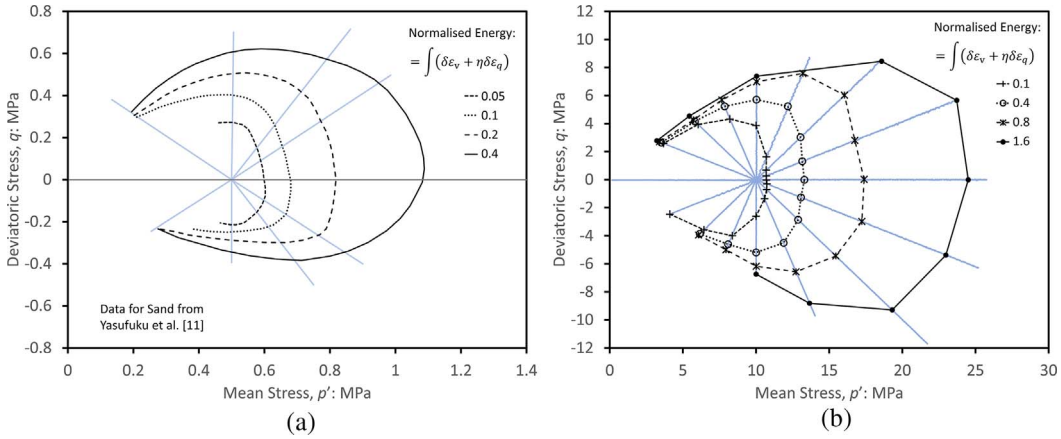

Fig. 14. Contours of normalised strain energy: experimental data (a) and DEM data (b).

of breakage is associated with compressive yielding at high stresses.

The outermost contour in Fig. 15(a) happens to correspond well with the ostensible yielding in Fig. 13(a), and these points are shown superimposed on the state-paths in Fig. 15(b). This e–p' plot shows clearly that only 5 of the simulations undergo compressive yielding, demonstrating a significant decrease in volume: 315°, 337.5°, 0°, 22.5°, 45°. The 67.5° and 292.5° tests, in which p' also increases, do not demonstrate as much crushing or demonstrate sudden or substantial volume reduction. This implies that a substantial amount of breakage is 'required' to facilitate a significant reduction in volume; the inner contours do not correspond with any obvious changes or kinks in the volumetric behaviour.

Furthermore, the (varying) levels of breakage in the simulations that yield at relatively low p' do not appear to have any major effects on the intrinsic η–ε_q shown earlier. A slight exception however is for the 67.5° simulation: in this case, the sample does not demonstrate major volume reduction, as it appears not enough breakage occurs. However, this test demonstrates more breakage than the remaining tests, and the η–ε_q response (Fig. 11) demonstrates slight divergence from the intrinsic η–ε_q curve. This could be described as intermediate behaviour, with enough crushing to affect the shear response but not enough to cause volumetric reduction.

Assuming that a certain or minimum amount of breakage is associated with compressive yielding, it will now be investigated what condition(s) give rise to such a degree of breakage at varying macroscopic stresses. The most obvious variable that can be analysed at compressive yield is some measure of average particle stress. If such a measure is a suitable indication of yielding, then one would expect that for a given (compressive) yield surface, this variable would take the same value at any point on the yield surface.

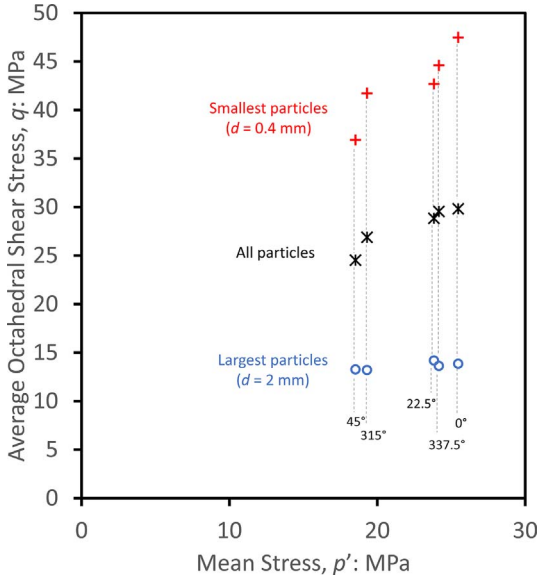

Fig. 16. Various measures of average particle stresses at yield.

Fig. 16 shows the average particles stresses measured at the yield

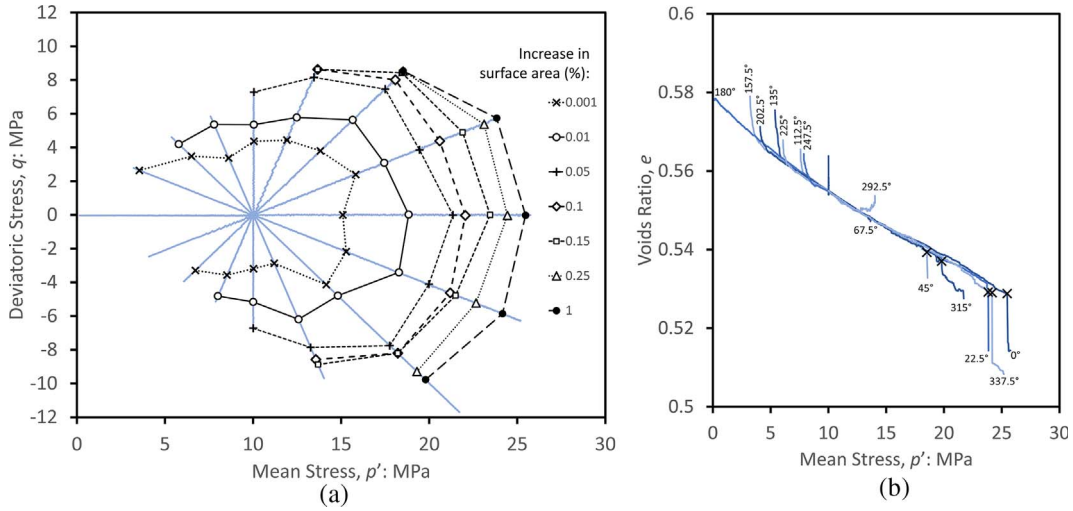

Fig. 15. Contours of constant surface area (a), and outer most points superimposed on state paths (b).

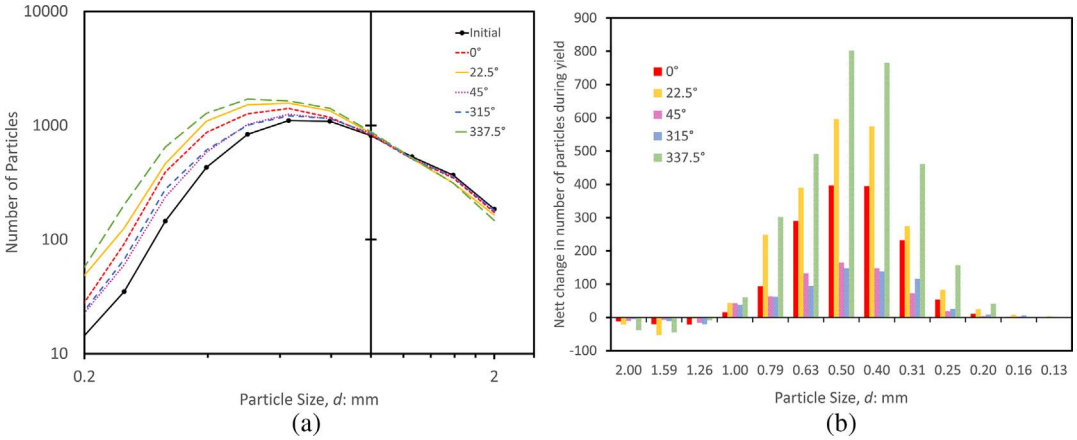

Fig. 17. Particle size distributions immediately following compressive yield (a), and net change in numbers of each size of particle during yield (b).

points marked in Fig. 15(b). Also shown are the average stresses in some of the finest (d = 0.4 mm) particles—the smallest particles are the strongest, are known to control the current voids ratio of an aggregate [30], and the strengths of such particles are often linked with increasing macroscopic stress. Neither of these show a constant value at the various yield points, rather it is the average stress in the largest particles that appears to take a constant value.

Inspecting the actual breakage taking place at these yield points reveals that breakage occurs across *all* sizes of particles, whilst pre-yield breakage only occurs in the relatively smaller sizes. Fig. 17(a) shows the particle size distributions immediately after the identified yield points, alongside the PSD of the initial sample at p' = 10 MPa—to which there are negligible changes to before yielding. Fig. 17(b) shows the overall change in the numbers of particles of each size, for the 5 tests that undergo compressive yielding. The largest sizes (e.g. 2 mm) show a decrease in quantity, whilst the smaller sizes show an overall increase. Although there is a difference between the simulations shown (e.g. the 337.5° simulation experiences more breakage than the 315° simulation), what is common and unique to these 5 simulations is that there is breakage across all sizes—therefore including the largest 2 mm particles, which (must) decrease in quantity at yield.

During compression of granular soil, a fractal particle size distribution emerges [30,31], which can be observed here by the developing linearity at the large end of the log-log plot in Fig. 17(a). It is generally understood that in such cases smaller particles—which are statistically stronger—must continuously break; whilst larger particles—which are much weaker—must remain largely intact. This phenomenon is often attributed to the effect of coordination number, whereby the largest and weakest particles are 'protected' by many contacts, whilst the smallest and strongest particles have few contacts, conducive to greater induced stresses. Additionally, the authors have shown that in such scenarios, it is the size of the smallest particles that determines the current voids ratio [30].

The results here indicate that compressive yielding, and therefore the associated decrease in voids ratio, is linked to crushing of all particle sizes, specifically including the largest. Plastic hardening on the normal compression line is caused by the smallest particles becoming stronger and stronger. However, to maintain the fractal distribution (and keep the correct ratio between sizes) as it evolves asymptotically to a semi-infinite fractal, relatively larger particles also need to break occasionally. Considering an established fractal size distribution and assuming a dimension of 2.5 (the value observed for soil and apollonian sphere packing [32]), this means for example that one particle of d = 2 mm must break for every ≈3000 particles of d = 0.25 mm that break. So whilst it is mainly the fine particles that must continuously break, proportional breakages must occur across all sizes to enable denser, more efficient packing and for there to be a decrease in voids ratio.

This is consistent with earlier work [33,34], which showed mathematically that an equal probability of fracture across all sizes leads to a fractal distribution, and in which case the substantial majority of breakages (and fragments) will be small. Considering the theoretical breakage of all fragments in an established, idealised fractal mixture, Palmer and Sanderson [33] noted that the special case of D = 2.5 occurs when each fragment size contributes equally and additively to a macroscopic crushing force.

What distinguishes this phenomenon from shear yielding, is that in the latter case, *only* the smallest particles break—this is therefore equivalent to abrasion, friction, wear and *not* bulk breakage of different sizes leading to the evolution of a fractal. Any stress path leading to a normally consolidated state through compressive yielding would require breakage that is still mainly the smallest grains, but breakage across other sizes too to maintain the fractal evolution.

4.2.4. Particle stresses

The results shown thus far suggest that although the majority of breakages upon yielding are of the finer particles, it is breakage of the largest particles that is unique to, and determines when compressive yield occurs. Fig. 16 suggests that there is a critical value of average stress in these largest particles that triggers yielding. This would imply that these measures of particle stress are a function of both q and p'—see the yield points identified in Fig. 15, the average stress in the largest particles is the same at both (p' = 18.5; q = 8.5 MPa) and (p' = 25.5; q = 0 MPa).

Fig. 18(a) demonstrates how the average stresses across various particle sizes increase during isotropic normal compression [5,30]. In general, the average shear stress in any given size of particle increases approximately linearly until there are numerous smaller particles in existence, which surround the larger particles, mitigating any further increases in stress. This process repeats itself for subsequently smaller particles, with the current smallest particles invariably bearing the greatest average shear stress. It is this phenomenon that leads to the evolution of a fractal particle size distribution. If the shear stress in particles continuously increased irrespective of relative size, then one would end up with the weakest (largest) particles continuously breaking and a constantly-uniform PSD, hindering any decrease in voids ratio. The key observation from this plot is that once there are enough smaller-sized particles, the average stress in the largest 2 mm particles appears to level-off and remains approximately constant for p' > 20 MPa.

Shown in Fig. 18(b) are the same measures of particle stress observed upon isotropic unloading. These data were retrieved from when the isotropically compressed sample was unloaded from 24 MPa to 10 MPa (before the overconsolidated stress-path tests). Despite the non-

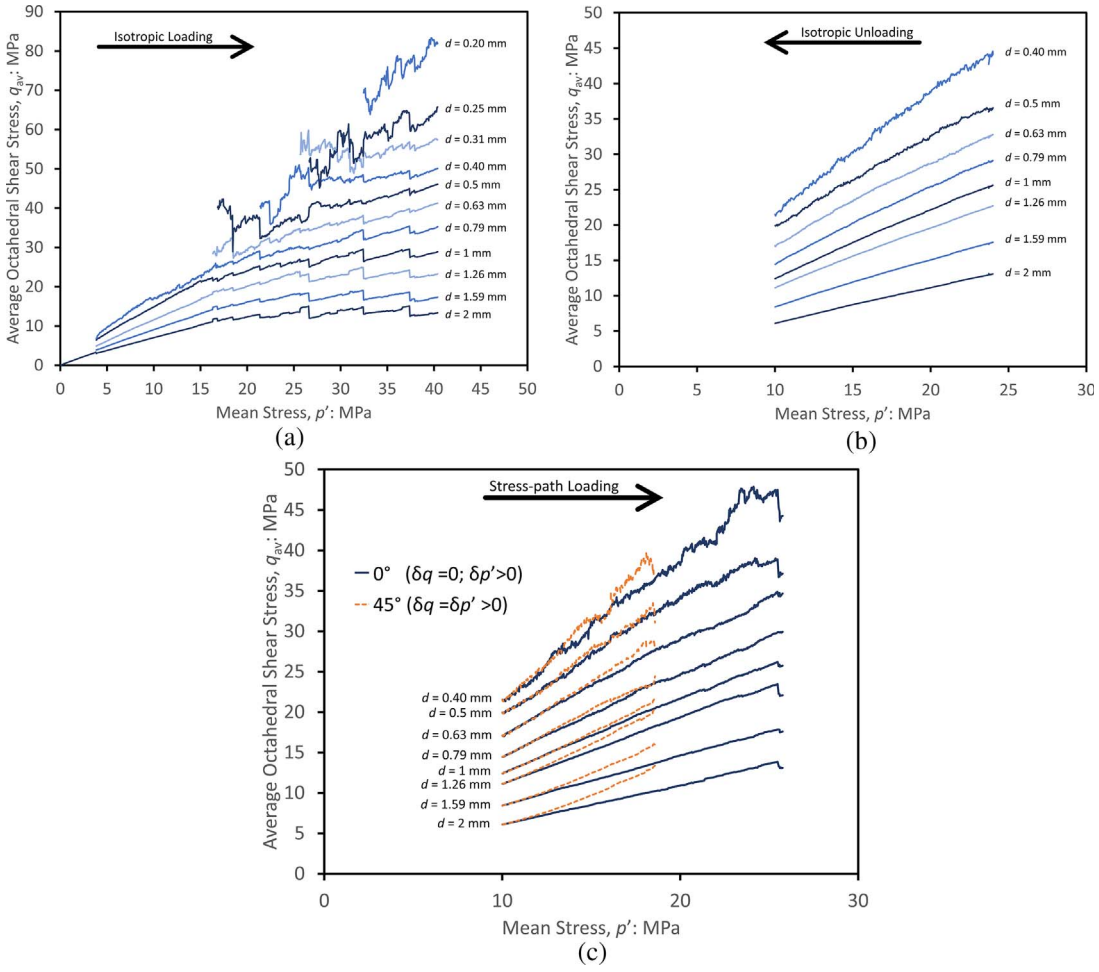

Fig. 18. Average particle stresses with respect to size during isotropic loading (a), isotropic unloading (b) and loading under various stress-paths (c).

linear behaviour observed during loading, upon unloading the particle stresses appear to be a linear function of the applied stress. Fig. 18(c) shows the equivalent data retrieved from 2 of the stress-path tests performed on the overconsolidated sample: 0° ($\delta q = 0$) and 45° ($\delta q = \delta p' > 0$). The average stresses in the isotropic (0°) test retrace the linear unloading paths (before reaching yield). Those from the 45° test however shows that the average stress in the largest particles increases non-linearly at an increasing rate (before yielding is reached). The largest particles bear greater stresses under deviatoric loading due to the force chain network in the assembly. In general, the largest particles in any loaded sample general carry the largest forces, partly due to their relative stability, but also in this case due to their ability to bear larger forces than their smaller counterparts (despite having lower strengths) [5]. For a quasi-static assembly, the magnitude of the largest contact forces will be proportional to the major principal stress. Hence, increasing q increases σ_1, producing larger contacts forces, the largest of which will be carried by the largest particles.

The effect of deviatoric stress on the average particle stresses is most pronounced in the largest particles, so much so that the average shear stress in these particles increases when p' reduces, shown in Fig. 19(a). The average stress in the largest particles, $q_{av,l}$ displays a net increase in most simulations, and increasing tendencies in all but the isotropic unloading test (180°). If this average particle stress is normalised by the current mean stress the effects of stress ratio are clear in Fig. 19(b). When elastic, increasing η causes the largest particles to carry larger shear stresses, and it appears it is the stress in these particles that must be large enough to initiate compressive yielding. The curvature in this plot is reflective of the curved compressive yield surface in q–p' space, and causes samples loaded with $\delta q \neq 0$ to yield at lower values of p'.

The stress-paths that undergo compressive yielding and substantial crushing reach approximately the same ultimate value of $q_{av,l}$. One would therefore expect the stress-states at which this ultimate value is reached to form a yield surface when plotted in q–p' space. Contours of constant $q_{av,l}$ are shown in Fig. 20, which appears to confirm this is the case when compared to Fig. 14(b) or Fig. 15(a). That the largest particles appear to reach an ultimate, steady value of average stress (Fig. 18a), implies that no further increasing contours are possible. What will be confirmed in later plots instead is that the outermost contour, representing the compressive yield surface, invariably corresponds to the limiting average particle stress of around 13–14 MPa. So for the same material but loaded to a much higher stress (e.g. $p' =$ 40 MPa), the yield surface would still coincide with a contour of average stress of about 13–14 MPa, and lesser contours would scale according between the origin and this limiting contour.

4.3. Effects of stress-history

4.3.1. Anisotropic stress history

The above results can now be compared to a further set of tests performed on an anisotropic initial sample. The compacted sample discussed to begin with was loaded isotropically to $p' = 10$ MPa prior to the stress-path tests. To achieve an additional sample on which to investigate, this compacted sample was loaded to $q = 8$ MPa, and then unloaded back to $q = 0$, whilst p' was held constant (Table 1). This set of simulations will be referred to as deviatoric, referring to its previous loading, to distinguish it from the results on the overconsolidated

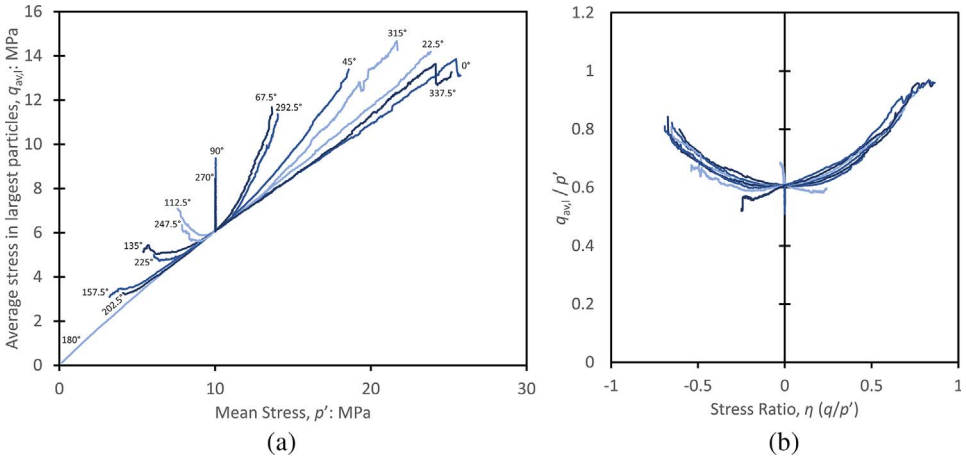

Fig. 19. Average stress in largest particles as function of mean stress (a) and normalised stress as function of stress ratio (b).

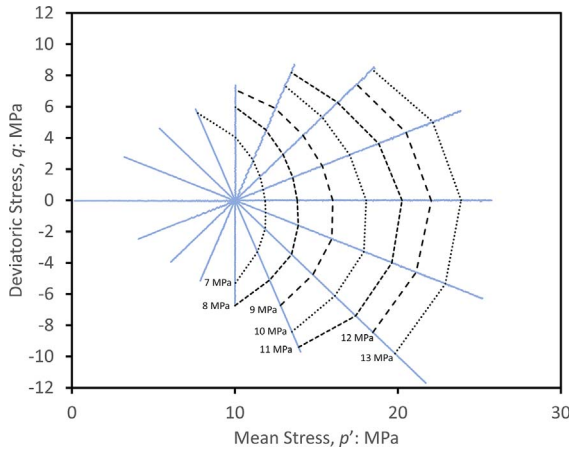

Fig. 20. Constant particle stress contours.

sample with an isotropic stress-history.

The state-paths from the three sets of tests are shown in Fig. 21(a). The deviatoric stress history has caused a small reduction in voids ratio, but compressive yielding, i.e. major volume reduction for this sample appears to occur at approximately the same p' as the compacted sample. This is also shown in Fig. 21(b), which shows the basic yield surfaces obtained for these results based on degradation of the bulk modulus. The yield surfaces for the compacted sample and that with the deviatoric stress-histories are similar, whilst the overconsolidated sample with an isotropic stress-history has a significantly larger yield surface. This shows that the deviatoric loading caused no significant volumetric hardening; despite resulting in permanent deformation, particle crushing and a reduction in volume.

Fig. 22(a) compares the stress ratio responses between the compacted and deviatoric-history samples. These plots clearly reveal an anisotropic response in the sample with a deviatoric loading history: the stress-paths in triaxial extension ($\delta q < 0$) display weaker (less stiff) behaviour, and those in triaxial compression display slightly higher stiffnesses. In both plots, a similarity can be seen for the tests which undergo compressive yielding (e.g. 0°, 22.5°, 337.5° etc), which yield at lower η compared to the remaining responses.

4.3.2. *Kinematic yielding*

The difference in stiffness depending on loading direction (or rotation of stress path) is very typical of soil, and is consistent with experimental data [10,35]. This type of behaviour is often visualised and understood via the use of kinematic yield surfaces, as shown by Jardine [22] and Kuwano and Jardine [21] for example, whereby an inner, highly-elastic yield surface is 'dragged' or translated around q–p' space within an outer yield/bounding surface. If this is the case, then for the sample that has previous deviatoric loading, the initial stress state at p' = 10 MPa would be located on the lower boundary of some inner elastic surface; stress-paths such as 270° are directed out of this boundary and are associated with low stiffness; whilst the 90° path is directed inwards and across this inner yield surface, and is associated with high stiffness.

An example is given from Jardine [22] in Fig. 23(a), which shows simple kinematic yield surfaces or 'small-strain zones' for a clay at two different states. This figure compares a one-dimensionally normally

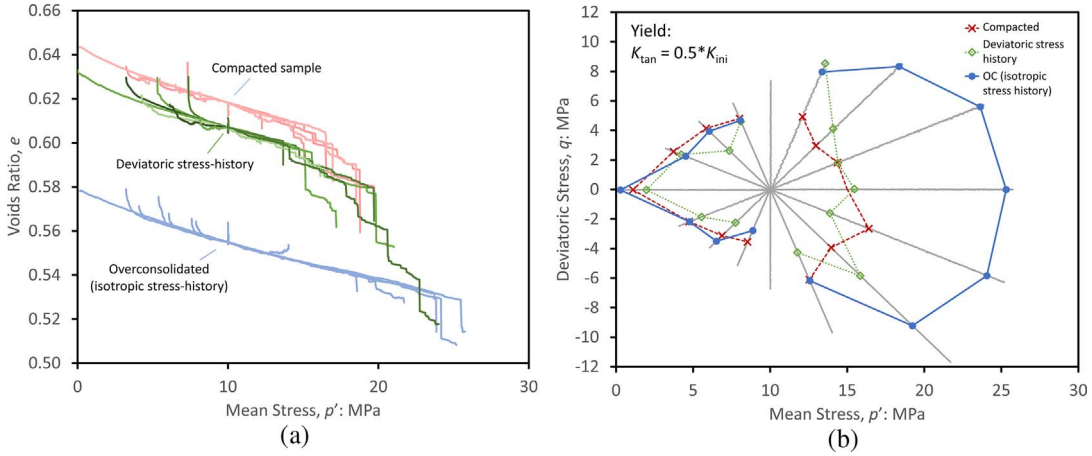

Fig. 21. State paths for the 3 different samples (a) and yield points according to K_{tan} (b).

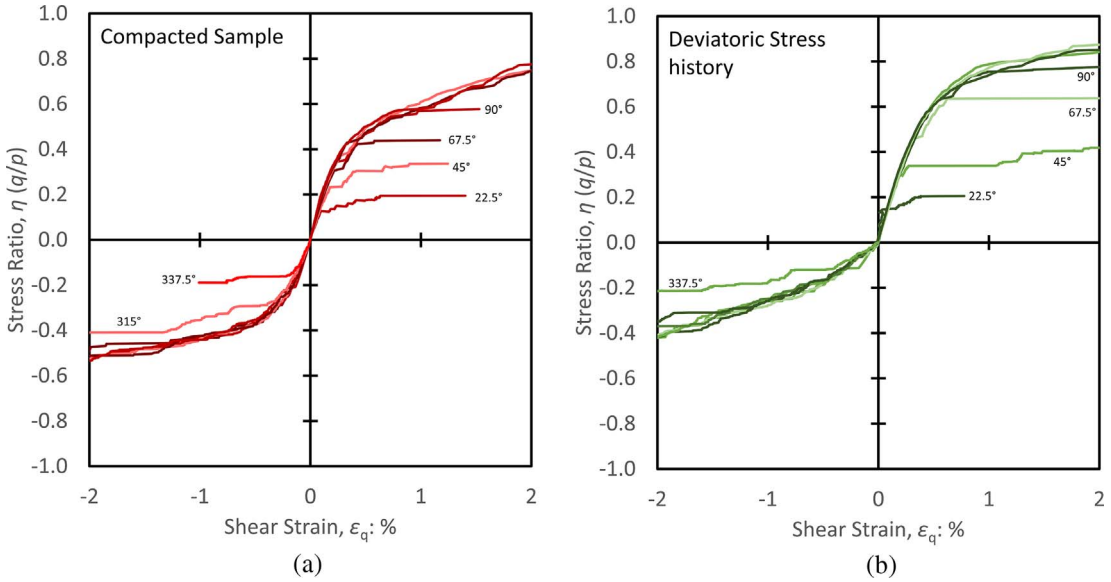

Fig. 22. Stress ratio versus shear strain for the compacted (a) and deviatoric (b) samples.

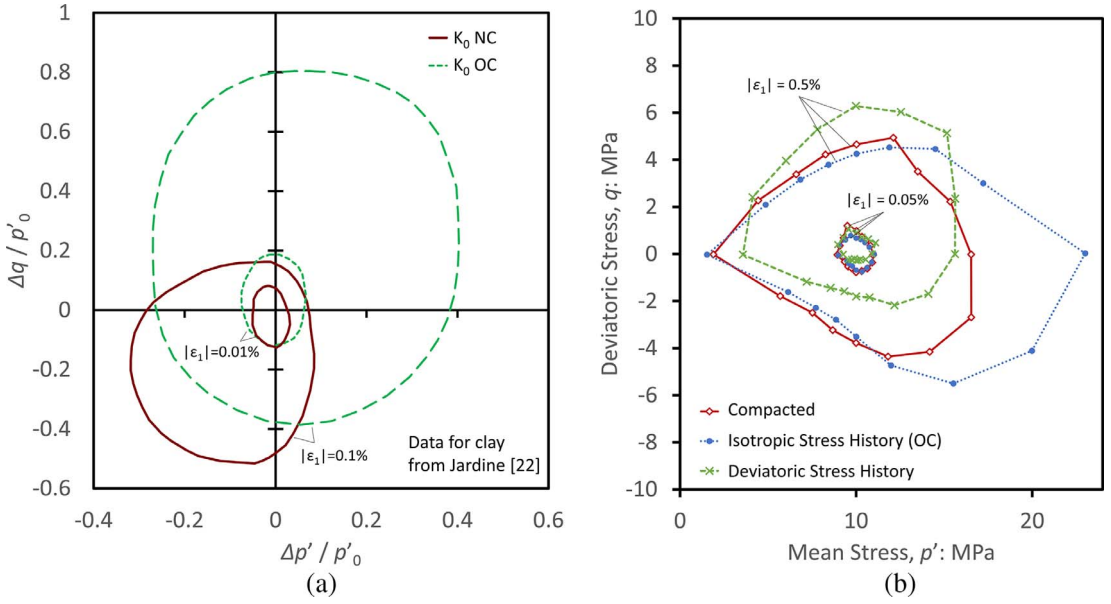

Fig. 23. Kinematic small-strain zones: experimental data (a) and DEM data (b).

consolidated state ($q \approx 200$ kPa; $p' \approx 270$ kPa) with a state that had been unloaded on a K_0 swelling line ($q = 0$ kPa; $p' \approx 100$ kPa). The two kinematic surfaces are defined in terms of constant (absolute) major principal strain ($|\varepsilon_1| = 0.01, 0.1\%$). It can be seen that for the sample that has been unloaded, the small-strain zones are greatly enlarged, particularly so in the direction of the previous loading path. Using similar measures of $|\varepsilon_1|$, regions are shown for the 3 sets of simulations in Fig. 23(b). Similar trends are visible in the DEM data, particularly for the sample with deviatoric history—both inner and outer zones are elongated in the upwards direction. There is negligible difference however between the inner zones for the compacted and overconsolidated samples, as both states are far from their respective yield surfaces.

4.3.3. Anisotropic crushing

Fig. 24 shows the contours of surface area for the tests on the compacted (a) and deviatoric sample (b). The values of these contours are chosen arbitrarily for the purpose of illustration; and note that the two sets of simulations have slightly different real initial surface areas. The contours for the compacted sample (much like those for the isotropically overconsolidated sample) are fairly isotropic about the p-axis. What Fig. 24(b) shows however is that for the sample with deviatoric stress-history, the inner contours (corresponding to minor breakage) are anisotropic. Initial breakage occurs rapidly upon loading in extension ($\delta q < 0$), whilst in triaxial compression ($\delta q > 0$) breakage occurs much later at greater applied shear stresses. The outer contour takes a more isotropic shape.

The innermost contour(s) in these plots represent a small increases in surface area, and can be interpreted as the first instances of breakage. Such small changes in surface area are only due to breakage of relatively small particles (breakage of larger particles is associated with much larger changes in surface area, not only due to their size, but also due to the fact that breakage of these particles invariably occurs together with breakages of all sizes of particles). It is the smaller particles that crush almost immediately upon loading in the $q < 0$ direction, causing the observed anisotropy in the η–ε_q responses.

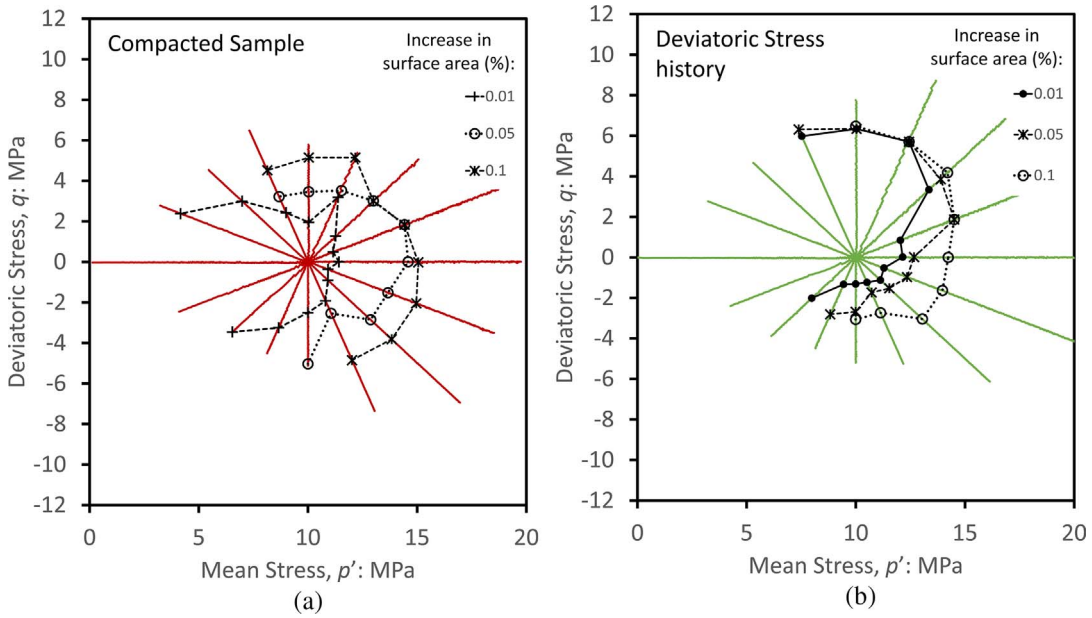

Fig. 24. Particle surface area contours for compacted (a) and deviatoric (b) samples.

For the sample with deviatoric history, why there is not much breakage occurring soon after loading with $\delta q > 0$ is due to any particles that are vulnerable to loading with $\delta q > 0$ already having been crushed during the previous loading. The term vulnerable particles here means those with minimal contacts, and therefore small, which upon strain would be subjected to rapidly increasing shear stresses and are likely to fail. This observation would imply that kinematic yielding and the dependence of stiffness on stress-path rotation observed experimentally is due to wear and abrasion—i.e. minor breakage of asperities and fine particles.

As for loading with $\delta q < 0$, there is more rapid breakage at smaller magnitudes of deviatoric stress. Comparing any two corresponding stress paths shows that the sample with a deviatoric stress-history has undergone more breakage at any given stress. Taking the 270° sample at $q = -5$ MPa for example, and comparing to at $q = 0$ MPa, shows that 22 of the original particles have undergone fragmentation; whilst for the compacted sample, this number is 7. Furthermore, a sizeable proportion of the particles that undergo fragmentation in the deviatoric case are those that were created during the prior deviatoric loading. This data is shown more clearly in Fig. 25.

Hence when subjected to triaxial extension ($q < 0$), whereby the radial direction becomes the major principal direction, there is accelerated particle crushing. The previous deviatoric loading results in such a packing whereby there are more particles vulnerable to high shear stresses upon radial loading. These appear to be primarily the new fragments produced in the previous loading to $q = 8$ MPa. These fragments are positioned transversely to the major principal stress, and any subsequent crushing of these newly-placed fragments, when the principal stresses are rotated, have a knock-on effect causing additional breakages due to contact force distribution.

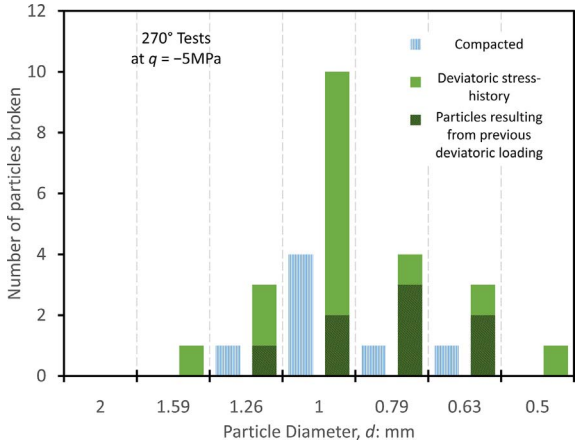

Fig. 25. Original particles broken in the two 270° tests at $q = -5$MPa.

4.3.4. Particle stress contours

It is difficult to quantify this 'memory' or anisotropy in terms of fabric when using spheres. Inspecting the orientation of contacts for example shows no clear distinction between the two initial samples with different stress-histories at $p' = 10$ MPa. If elongated particles were used however, which would be more susceptible to induced stresses in a particular direction, one would expect to observe different particle orientations following loading and unloading in one particular direction. However, mapping out contours of average particle stress gives some indication of the difference between the samples. In the compacted and deviatoric samples only the first 4 sizes of particle (2, 1.59, 1.26, 1 mm) have developed to quantities large enough to obtain reliable measures. Fig. 26 shows the contours of average particle stress from the stress-path tests on these two samples, for the largest (2 mm) and smallest (1 mm) sizes.

For the compacted sample (a), contours of stress for both largest and smallest sizes are centred on and symmetrical about the p-axis. For the sample with deviatoric history (b), this is only the case for the largest particles(i), the contours for the finer particles (ii) are anisotropic. For these 1 mm particles the contours are more 'stretched' in the $q > 0$ direction. The 90° stress-path (retracing the previous loading path) does not cross any contours. In general for the deviatoric sample, the average shear stress in the finer particles increases less rapidly with q. Conversely, when loading with $\delta q < 0$ shear stresses are induced more rapidly in these finer particles compared to the (isotropic) compacted sample, causing accelerated breakage.

It therefore appears that the average stress in the finer particles is influenced by the stress history. For the (isotropic) compacted sample, the contours are centred on the p-axis, whereas for the deviatoric sample these contours are skewed or tilted towards the path of previous loading, showing a form of rotational hardening. It is breakage of these finer particles that gave an earlier indication of shear yielding, and the difference in these contours seems to explain the observed anisotropy in

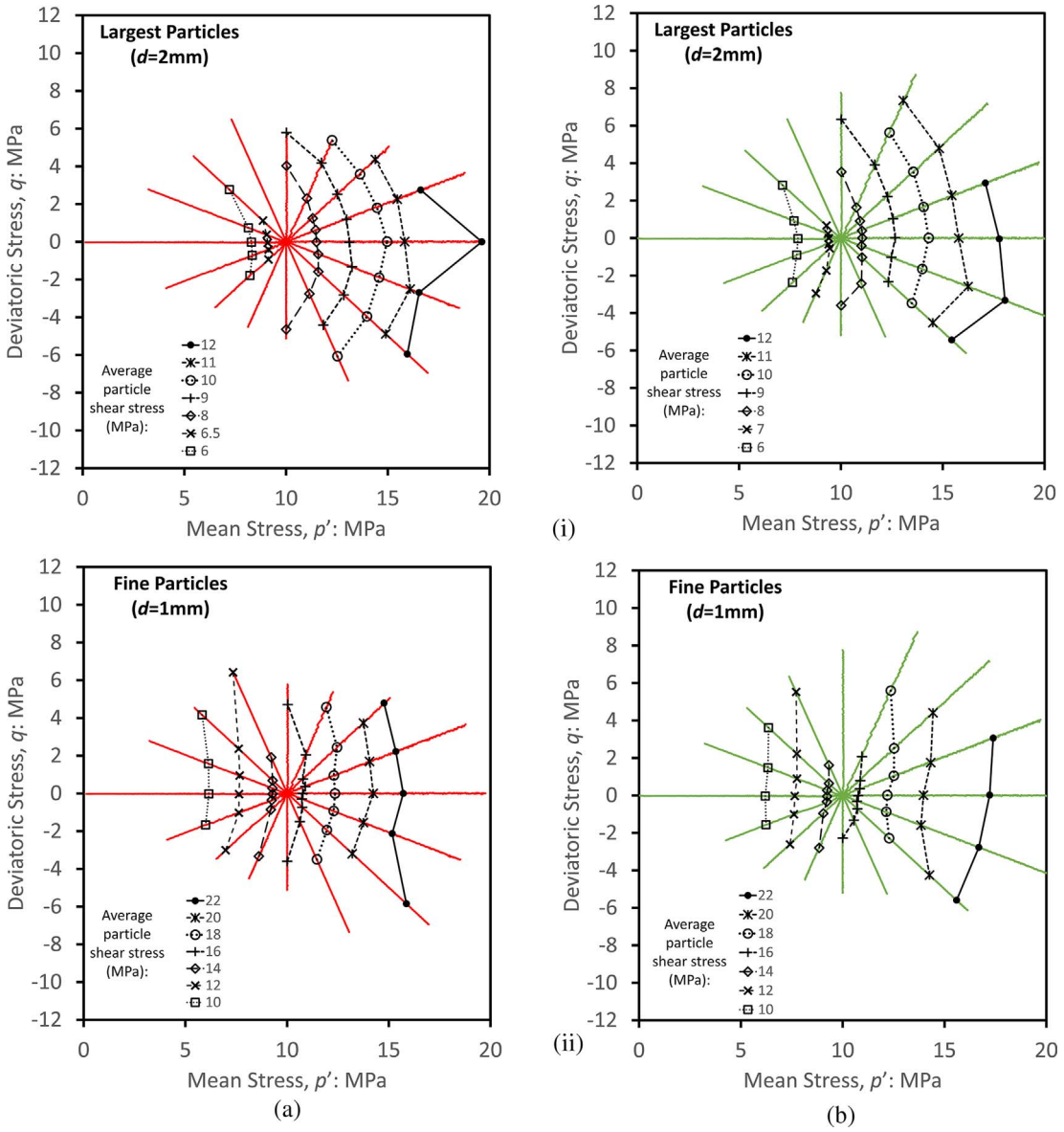

Fig. 26. Particle stress contours in the compacted sample (a) and deviatoric stress-history sample (b). Contours represent average shear stress in the largest (i), and smallest (ii) particle sizes.

the shear responses.

In contrast the average stresses in the largest particles are uninfluenced by the previous loading; the contours are centred on the p-axis regardless of any anisotropic stress-history. It was speculated earlier that it is breakage of the largest particles that is linked to compressive yielding, and that the compressive yield surface could therefore be approximated by contours of average stress in the largest particles. If this is the case, then these results suggest that any compressive yield surface is isotropic, and its shape or orientation is uninfluenced by anisotropic stress-history.

4.4. Normally consolidated states

4.4.1. Isotropic

Two final sets of stress-path tests will now be shown, both of which are performed from normally consolidated states at high stresses, assumed to be plastic and on normal compression lines, but with different stress-histories. The first set uses a sample that has been isotropically compressed to $p' = 24$ MPa. This sample consists of 5551 particles, with $e = 0.53$ and $d_{min} = 0.2$ mm. The stress ratio responses for these tests are shown in Fig. 27(a), and here it can be seen that more of the tests yield at lower stress ratios compared to the previous cases—e.g. the 112.5° and 135° tests. For the $\delta\eta > 0$ tests, only the 157.5° (and possibly the 135° test) appear to follow an intrinsic curve. As shown in Fig. 27(b), which shows the volumetric behaviour in terms of e and p', even the 112.5° test appears to reach the compressive yield curve and undergo volumetric compression, despite p' decreasing.

Fig. 27(b) shows that all tests in which $\delta p' > 0$ experience yielding immediately upon loading; there appears to be no elastic region beyond $p' = 24$ MPa. This behaviour is consistent with the initial state being located at the apex/tip of the yield surface in q–p' space, as should be the case if the compressive yield surface is isotropic.

Particle stress contour plots obtained from these simulations are given in Fig. 28. Shown here are contours of average stress for the largest (2 mm), intermediate (1 mm), and the smallest particles (0.4 mm), the latter being the smallest size for which there are a reliable quantity of particles to obtain an average (there are always very few of the finest particles, regardless of their actual size, due to the evolving nature of the PSD). The outermost, limiting contour for the largest particles (a) corresponds to the same value of average shear stress as

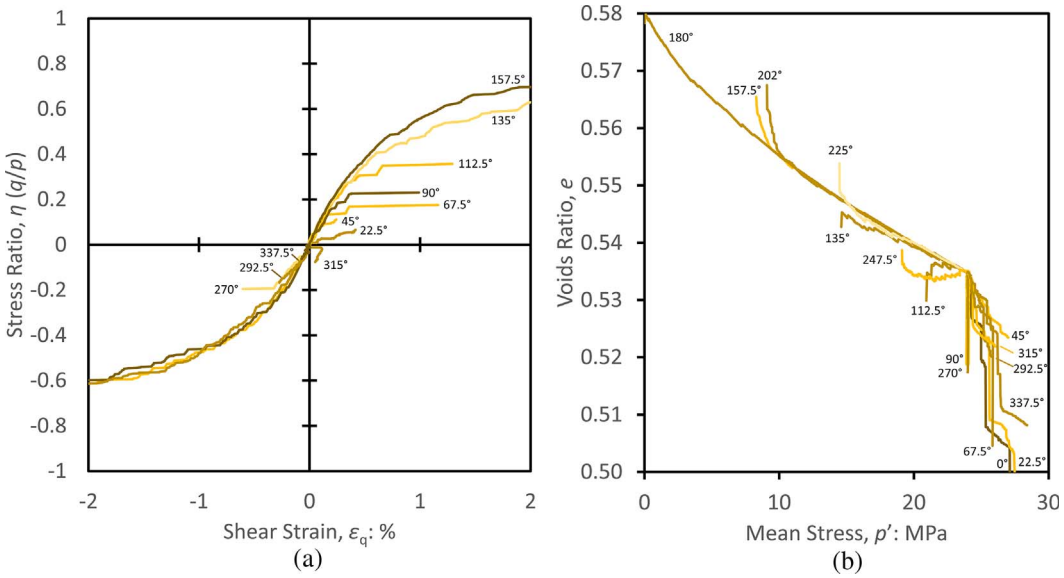

Fig. 27. Stress ratio responses (a), state paths in *e–p′* space (b) for the isotropically normally consolidated sample.

previously.

The contours for the largest 2 mm particles appear centred on the mean stress axis and symmetrical. Interestingly, the contours for the intermediate particles (b) appear almost vertical and not influenced significantly by the applied deviatoric stress; but simply a function of *p′*. Shown in (c) are the stress contours for the finest particles, and in this case the average stress displays more dependence on *q*; the contours overall display a slight curvature centred about the *p*-axis. Although this curvature is not as eminent as the largest particles, it can be seen that increasing *q* alone results in an increase in the average stress in these particles.

4.4.2. Anisotropic

The final set of stress path tests were performed on an anisotropic

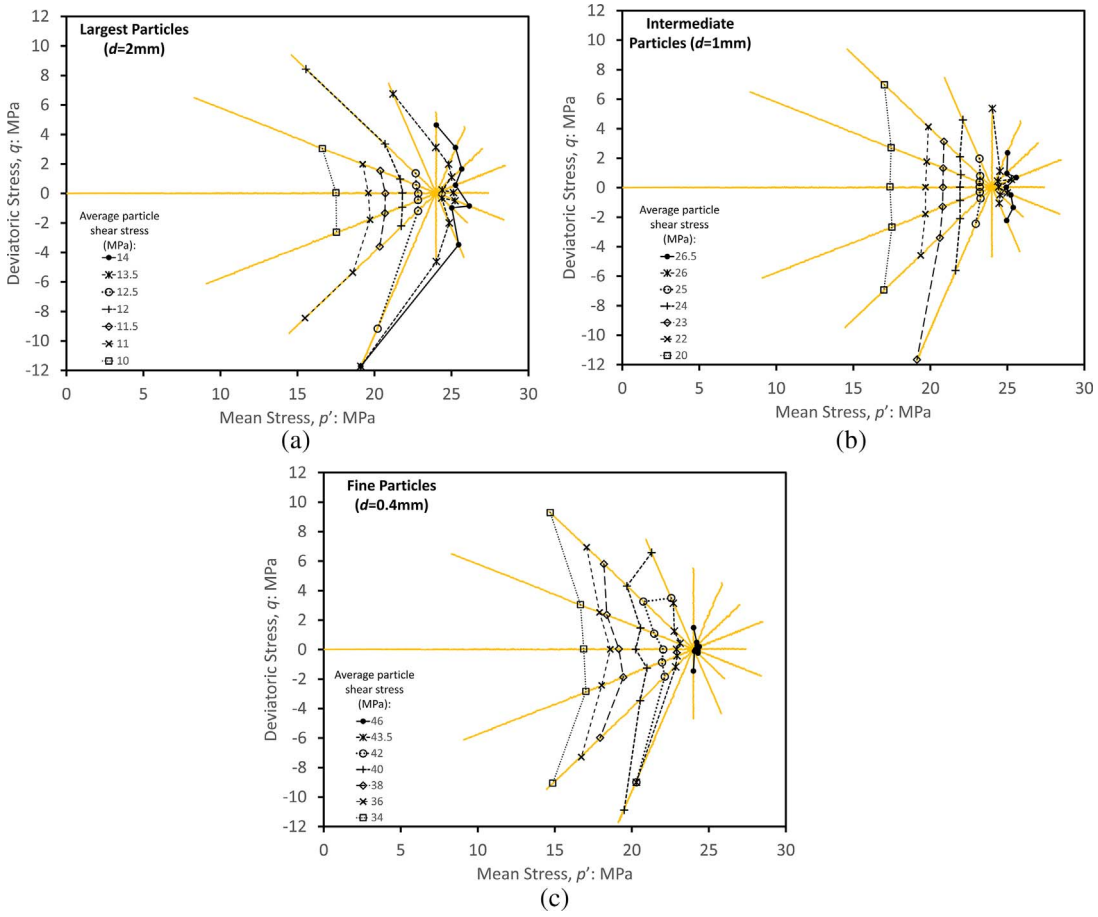

Fig. 28. Average particle stress contours for the isotropically normally consolidated sample, for the largest (a), intermediate (b) and fine particles (c).

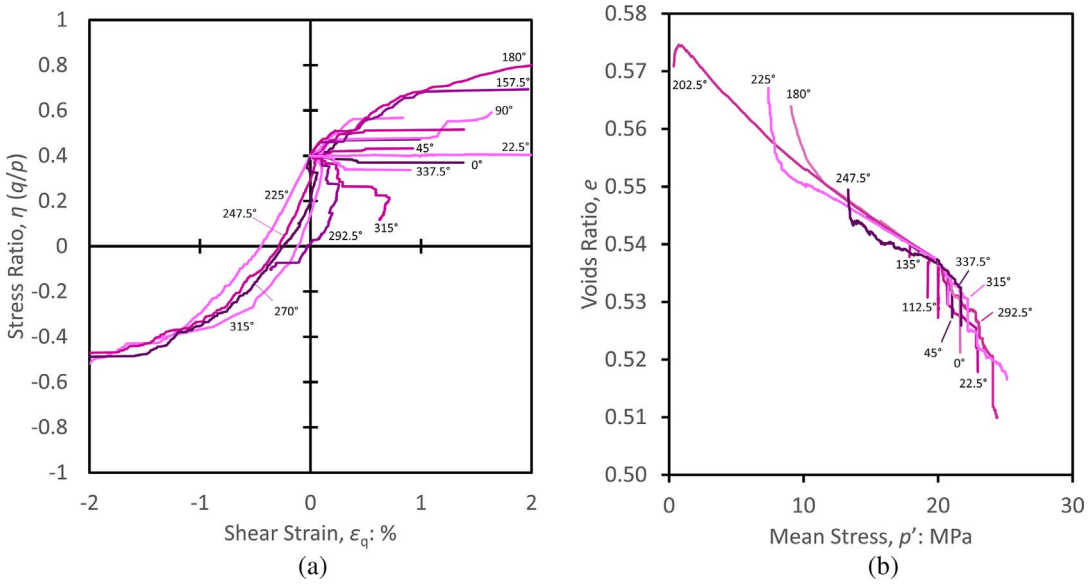

Fig. 29. Results from the anisotropically normally consolidated sample: stress ratio versus shear strain (a), volumetric behaviour (b).

normally compressed sample, compressed with a constant stress ratio $\eta = 0.4$ to $q = 8$ MPa, $p' = 20$ MPa. This sample has 6004 particles, $e = 0.54$ and $d_{min} = 0.16$ mm. The stress ratio responses are given in Fig. 29(a), and the behaviour here appears to be dominated by the effects of particle crushing. Ordinarily, increasing the stress ratio would lead to increasing shear strain and progressive, frictional yielding, unless particle crushing occurs. In this plot, only the 180° stress-path appears to demonstrate such behaviour, for all other tests in which $\delta\eta > 0$, crushing and therefore yielding occurs at lower stress ratios—and immediately for those in which p' increases or remains constant (e.g. 45°, 90°).

Similarly, by decreasing η, one would expect negative shear strains to accrue and ultimately frictional/shear yielding. Only the 225° simulation demonstrates a monotonic decrease in shear strain. For the simulations in which η decreases but p' increases rapidly (0°, 337.5°), particle crushing occurs almost immediately upon loading as the sample undergoes compressive yielding. The imposed stress ratios ($\eta > 0$) at the points of compressive yield cause significant shear strains to occur.

For the tests in which η decreases and p' remains constant or decreases (e.g. 225°–270°), the *overall* trend is for the shear strain to decrease. However the behaviour includes sudden, transient positive shear strains occurring due to minor breakage. This plastic behaviour, in particular for 270° case in which p' is held constant and the shear stress reduced, is indicative of an anisotropic/rotated yield surface, for which the apex is not centred on the p-axis [11].

The volumetric behaviour for these tests is shown in Fig. 29(b). It is quite clear from first glance that volumetric yielding occurs for all simulations in which p' increases.

Kuwano and Jardine [21] presented contours of constant shear and volumetric strain for a sand with a similar (anisotropic) loading history but at lower stresses. Their contours of constant ε_q and ε_v are shown in Fig. 30; comparable simulation contours are given in Fig. 31. For the experimental data, the ε_q contours in Fig. 30(a) are broadly aligned with the loading path (or η), and approximately radiate from the origin. For the DEM data in Fig. 31(a) however, the decreasing (negative) ε_q contour slopes downwards at large p', and shows no correlation with η. This however should be expected from the shear responses shown in Fig. 29(a), and is due to breakage occurring immediately for the simulations in triaxial extension. As shown earlier, this breakage, occurring under a positive imposed stress ratio, causes instances of positive shear strain, despite η decreasing. Hence this difference with experimental data can be attributed to the stress level.

There appears better agreement when comparing the ε_v contours in Figs. 30(b) and 31(b). Broadly, in both plots the contours of ε_v are roughly vertical, showing correlation with p'. Additionally, in both plots the contours are curved around the original state such that loading with constant-p' causes positive volumetric strain.

Fig. 32(a) shows contours of increasing surface area from these simulations, which show breakage occurring in nearly all stress-path directions. The surface area increases most rapidly in those tests in which q or p' increases, and particularly so when both increase. The inner contours demonstrate the most anisotropy, whilst the outermost contour takes a more isotropic shape. The inner contours appear rotated compared to the isotropic normally-consolidated sample, however as noted, the inner contours represent breakage of the finer particles. With continuing breakage, the actual increase in surface area will become dominated by the contribution from the largest particles crushing, and the observation that the outermost contour is more-or-less isotropic also supports the proposition that breakage of the largest particles is uninfluenced by anisotropic stresses. Such data is unavailable from experimental testing, however, the contours of cumulative work obtained from the simulations are very similar, and demonstrate the same trend. Fig. 32(b) shows such contours obtained from a clay with similar loading history, and in both cases the same trend is observed whereby the contours tend to become more isotropic.

The microscopic behaviour and precise nature of yielding that takes place in the 270° stress-path is of particular interest, as this simulation will give a definitive indication of the shape or orientation of the yield surface for the anisotropic sample. This simulation demonstrates breakage very soon after the start of the stress path, but as revealed in Fig. 32(a), a much greater length of stress path must be traversed to achieve a given amount of breakage compared to one of the tests in which q or p' increases (e.g. 0–90°).

Fig. 33 shows the particle stress contours for the largest, intermediate, and finest particles. The contours for the largest particles (a) are again centred on the p' axis, the same as all other tests on samples with different stress-histories. Hence, there is no effect from the anisotropic loading. If these contours are isotropic, and are indicative of compressive yielding as proposed, then one would expect the 292.5° and 315° stress-paths should undergo compressive yield at the highest p'. This is supported by Fig. 29(b), which indeed shows that the 292.5°, 315° and 337.5° demonstrate the 'latest' yielding at slightly higher p' than the other simulations.

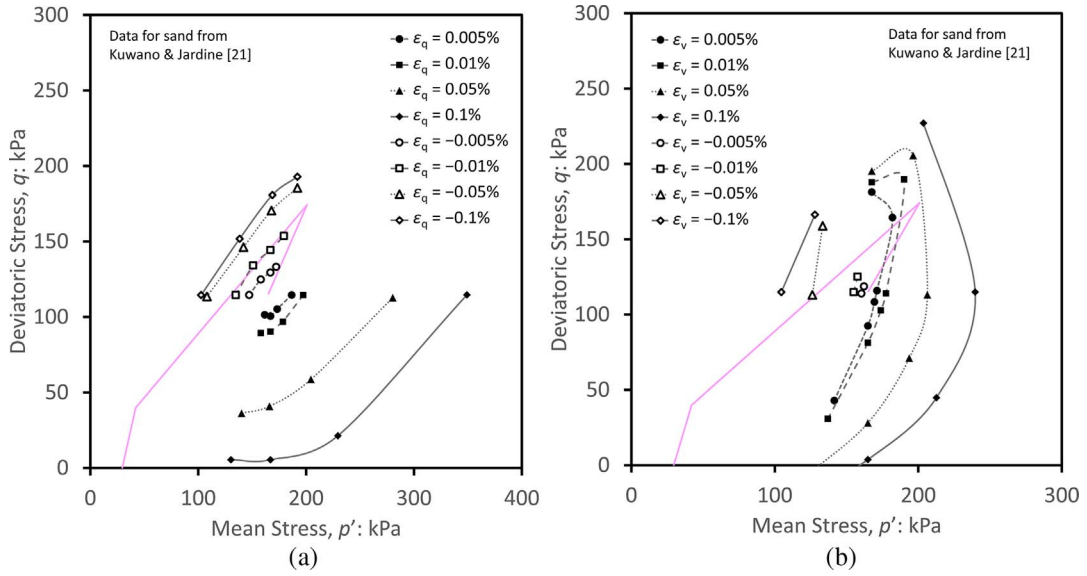

Fig. 30. Experimental contours of constant shear strain (a) and volumetric strain (b) for a sand from Kuwano and Jardine [21]

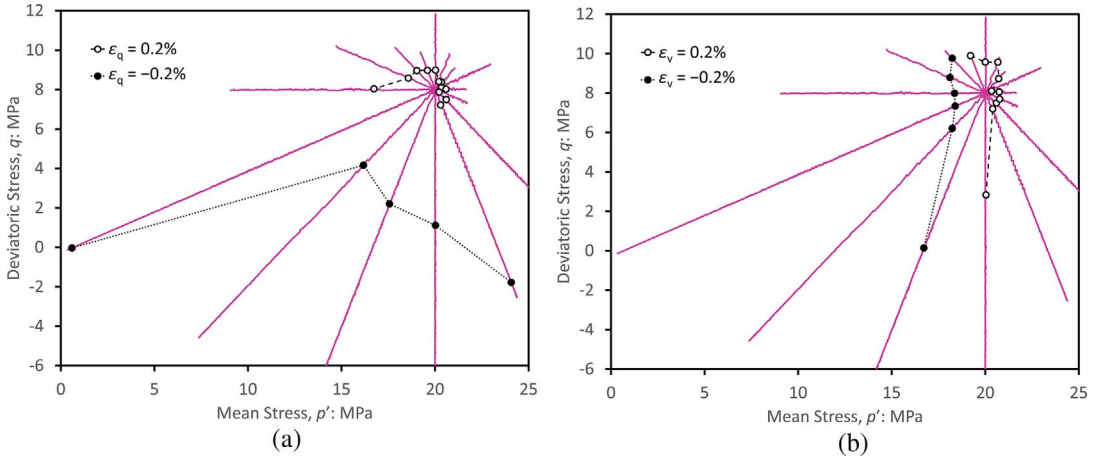

Fig. 31. Simulation contours of constant shear strain (a) and volumetric strain (b).

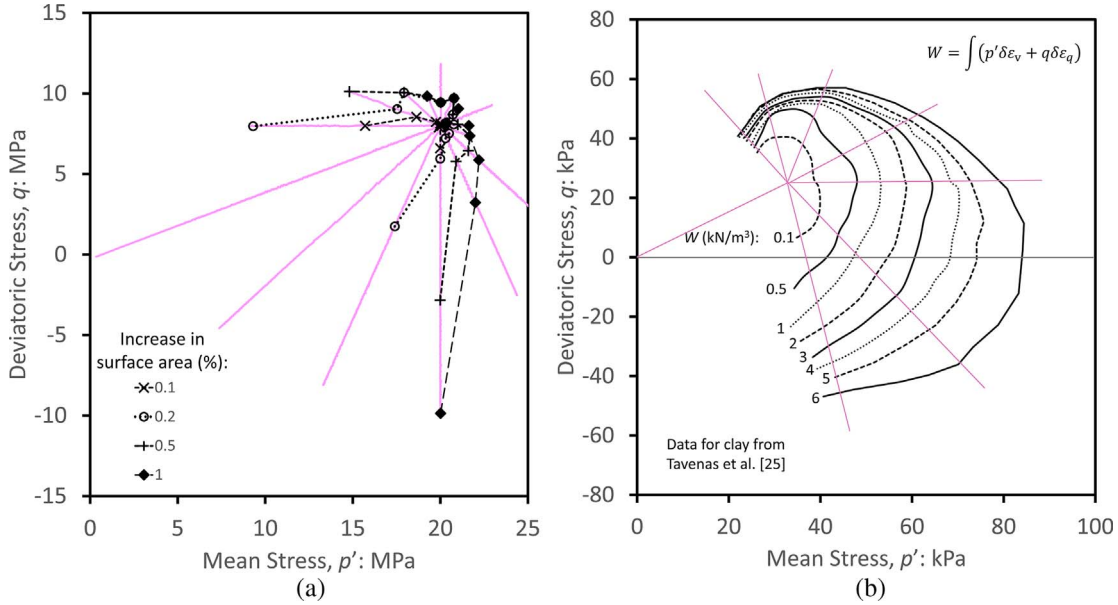

Fig. 32. Contours of surface area from simulations (a) and cumulative work contours for a clay with similar stress history (b).

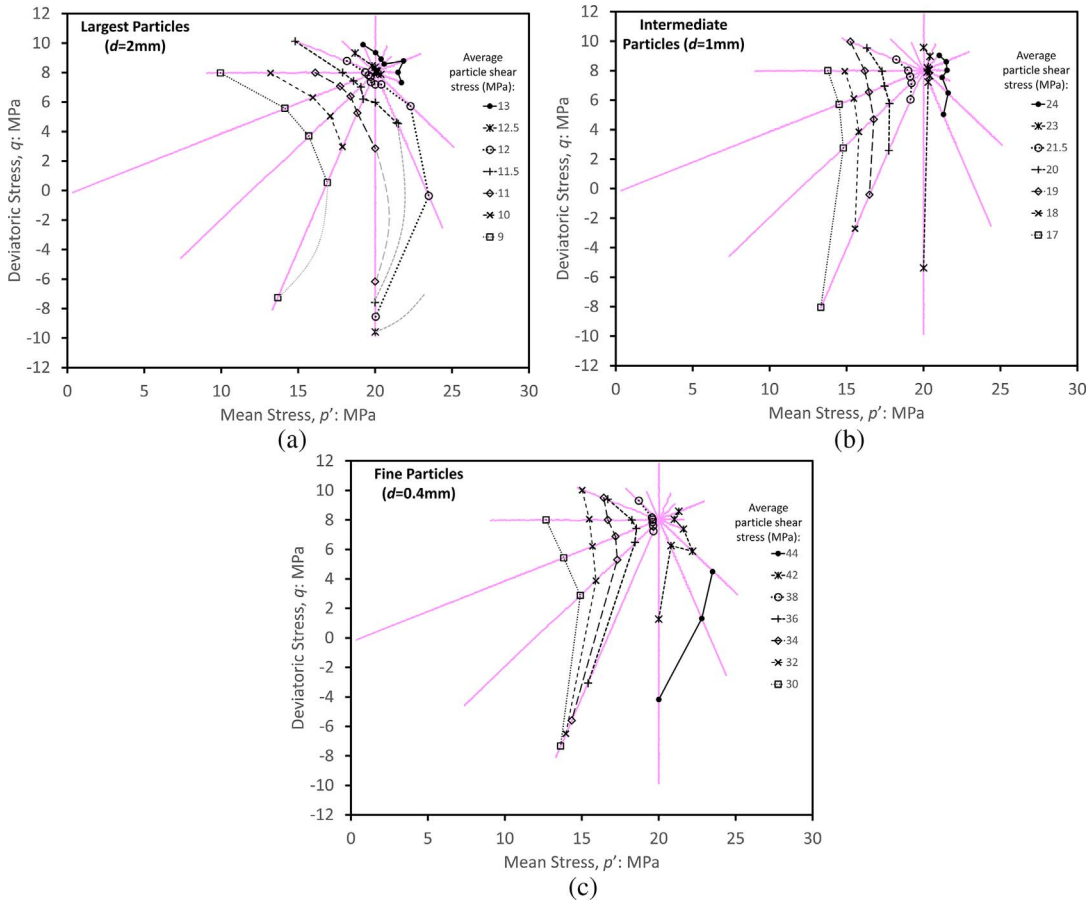

Fig. 33. Average particle stress contours for the anisotropically normally consolidated sample, for the largest (a), intermediate (b) and fine particles (c).

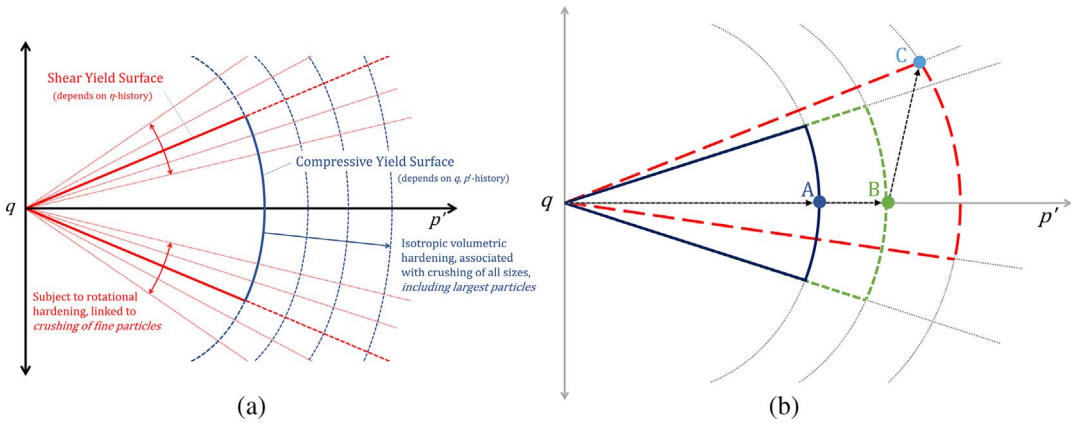

Fig. 34. Schematic illustrating separate yield surfaces (a) and example stress path and hardening (b).

The average shear stress in the intermediate particles tends to show much less dependence on q and the contours are more vertical. The contours for the fine particles however appear to be directly influenced by the stress history, these contours appear centred on the previous stress path; aligned with the line $\eta = 0.4$. That is, these contours of average stress are rotated compared to the isotropic case (Fig. 28c). The anisotropy demonstrated in this plot can explain the observed anisotropic macroscopic shear responses in Fig. 29(a), specifically that unloading q at (or nearly) constant p' produces increasing octahedral shear stresses in the relatively fine particles causing breakage. However, crushing of these fine particles alone does not contribute to or cause macroscopic compressive yielding, which is dependent on the largest particles crushing, and only affects the shear responses.

4.5. Idealised behaviour

In summary, it therefore appears that it is the finest particles that control the shear yield surface, and it is crushing (or damage) of such particles that is responsible for any observed anisotropic or kinematic yielding. The compressive yield surface meanwhile is controlled by the largest particles, which must break (along with all other sizes of particles) to cause volumetric compressive yielding. This proposition is illustrated in Fig. 34(a). Fig. 34(b) demonstrates an example stress path: after isotropic loading to point A, subsequent loading from A to B results in isotropic hardening, whereby the compressive yield surface moves but has no effect on the shear yield surface. Loading from B to C however causes the shear yield surface(s) to rotate anti-clockwise.

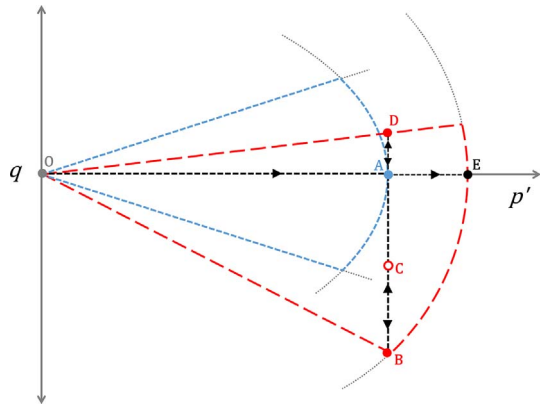

Fig. 35. Schematic diagram showing stress path test performed on heavily crushed sample.

To further illustrate the proposed yield surfaces and hardening, as well as provide additional evidence for the observations already made, a further, more elaborate stress-path simulation was performed on the heavily crushed, isotropically normally consolidated sample. From the isotropic state of $p' = 24$ MPa, the sample was loaded with a negative shear stress, to $\eta = -0.6$. This is shown schematically in Fig. 35, and corresponds to the path AB. The initial state (A) is on the tip of the compressive yield surface, so this loading should result in instantaneous compressive yielding in addition to shear yielding. This results in both an expansion of the compressive yield surface, and (kinematic) rotation of the shear yield surfaces. To demonstrate the latter, the sample is then unloaded from point B to point C, then reloaded back to point B. During reloading (CB), minimal crushing should occur, as the path BCB is within the new elastic region. Afterwards, the sample is subjected to a positive shear stress ($q > 0$) until yielding again at point D, which is expected to occur at a small (positive) η, due to rotation of the shear yield surface.

The sample is then taken back to an isotropic state (point A), and isotropically compressed until reaching compressive yield. The new isotropic yield stress (point E) should be greater than 24 MPa due to the

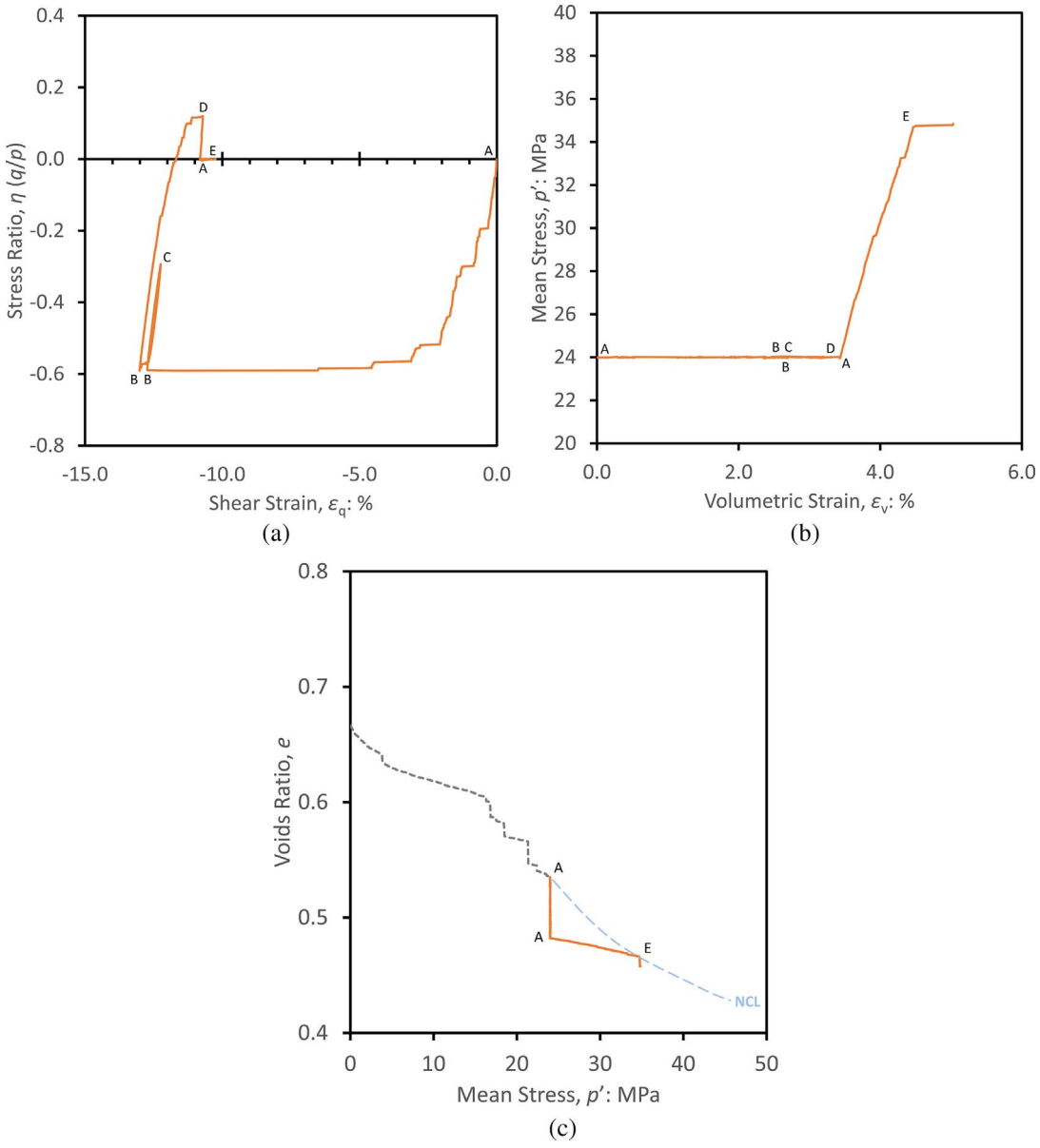

Fig. 36. Stress strain responses for heavily crushed stress path simulation: deviatoric behaviour (a), volumetric behaviour (b) and *e*–*p* response (c).

initial compressive hardening experienced when loaded from B to C, despite the mean stress p' remaining constant during this time.

The deviatoric, volumetric, and e–p' responses for this stress-path simulation are shown in Fig. 36, which confirm that the sample exhibits behaviour as expected. During the first loading from A to B, the number of particles increases from 5551 to 14,591, and then to 18,895 at point E. The deviatoric response in Fig. 36(a) reveals plastic behaviour immediately upon loading from A to B, which is followed by evidently more stiff, elastic behaviour between points B, C, B. Loading to positive shear stress results in plastic strains beginning to occur at a noticeably low stress ratio ($\eta < 0.2$). The volumetric response in Fig. 36(b) shows that despite no increase in p', positive volumetric strain occurs when loaded deviatorically, especially initially from A to B, as the stress state is on the (expanding) compressive yield surface. Significantly, the final path from A to E shows stiff, primarily elastic behaviour before once again yielding at a larger p'. This is also shown in Fig. 36(c), which shows the e–p' behaviour, where it can be observed that this latter yielding, at $p' \approx 35$ MPa, is when the state re-joins the normal compression line.

5. Conclusions

Sets of stress-path tests have been performed on a numerical soil to explore the yield surface in q–p' space and investigate the underlying micro mechanics. Much like real granular soil, the DEM sample demonstrated two distinct types of yielding depending on stress level. At low mean effective stresses, the soil underwent frictional 'shear' yielding, whilst at high stresses, the samples exhibited major particle crushing and underwent 'compressive' or volumetric yielding.

Yielding at low stresses appeared to be a function of stress ratio, whilst at high stresses, the frictional behaviour was superseded by crushing as the samples underwent compressive yielding. Compressive yielding was caused by the onset of major crushing, and it was shown that this involved the fragmentation of particles of all sizes, this specifically included the largest particles (although only very few).

For a sample subjected to loading under some combination of stresses, but prior to compressive yielding, particles of relatively smaller sizes may break, but this does not have any noticeable effect on the volumetric stress-strain behaviour. However, breakage of the relatively fine particles may noticeably affect the shear stress-strain behaviour, causing accelerated shear strain and an earlier appearance of yielding.

Contours of average particle stresses were shown in q-p' space for various samples, and it was revealed that for the largest particles, such contours of stress were curved and isotropic about the p-axis, regardless of stress-state or loading history. It was found that it is the breakage of these largest particles (accompanied by many further breakages of finer sizes) that is unique to or causes major compressive yielding and enables the associated reduction in volume. As such, the compressive yield surface at high stresses, like the contours of average stress, were shown to be isotropic and did not undergo any rotation or change in shape. The stress in these largest particles was a function of both q and p', and reflect the curvature observed in the yield surface at large p' in q–p' space.

Contours of stress for the relatively fine particles however demonstrated rotation depending on the prior loading path(s). A sample loaded with a constant stress ratio ($\eta > 0$) revealed contours of constant stress that were centred on the previous loading path. Likewise, an isotropic sample that was subjected to deviatoric loading and then unloading ($q = 0 \rightarrow 8 \rightarrow 0$ MPa), showed anisotropic contours, and demonstrated anisotropic macroscopic responses, with the shear stiffness depending on the direction of the stress-path, much like what is observed for real soil and often explained using the concept of kinematic yield surfaces.

All anisotropic behaviour resulting from stress-history was only observed in the shear responses, and could be attributed to breakage of the relatively fine particles, whilst the stresses in the largest particles, and therefore compressive yielding remained isotropic regardless of loading history.

Acknowledgements

This work was supported by the Engineering and Physical Sciences Research Council [grant number EP/L019779/1].

References

[1] McDowell GR, de Bono JP. On the micro mechanics of one-dimensional normal compression. Géotechnique 2013;63:895–908. http://dx.doi.org/10.1680/geot.12.P.041.
[2] McDowell GR, de Bono JP, Yue P, Yu H-S. Micro mechanics of isotropic normal compression. Géotechnique Lett 2013;3:166–72. http://dx.doi.org/10.1680/geolett.13.00050.
[3] de Bono JP, McDowell GR. Micro mechanics of drained and undrained shearing of compacted and overconsolidated crushable sand. Géotechnique 2017;Published:1–15. http://dx.doi.org/10.1680/jgeot.16.P.318.
[4] Itasca. PFC3D; 2015.
[5] de Bono JP, McDowell GR. Particle breakage criteria in discrete-element modelling. Géotechnique 2016;66:1014–27. http://dx.doi.org/10.1680/jgeot.15.P.280.
[6] McDowell GR. On the yielding and plastic compression of sand. Soils Found 2002;42:139–45.
[7] Bandini V, Coop MR. The influence of particle breakage on the location of the critical state line of sands. Soils Found 2011;51:591–600.
[8] Coop MR. The mechanics of uncemented carbonate sands. Géotechnique 1990;40:607–26. http://dx.doi.org/10.1680/geot.1990.40.4.607.
[9] Chandler HW. A plasticity theory without Drucker's postulate, suitable for granular materials. J. Mech. Phys. Solids 1985;33:215–26. http://dx.doi.org/10.1016/0022-5096(85)90012-2.
[10] Wood DM. Soil behaviour and critical state soil mechanics. Cambridge University Press; 1990.
[11] Yasufuku N, Murata H, Hyodo M. Yield characteristics of anisotropically consolidated sand under low and high stresses. SOILS Found 1991;31:95–109. http://dx.doi.org/10.3208/sandf1972.31.95.
[12] Smith PR, Jardine RJ, Hight DW. The yielding of Bothkennar clayGéotechnique 1992;42:257–74. http://dx.doi.org/10.1680/geot.1992.42.2.257.
[13] Cheng YP, Bolton MD, Nakata Y. Crushing and plastic deformation of soils simulated using DEM. Géotechnique 2004;54:131–41. http://dx.doi.org/10.1680/geot.2004.54.2.131.
[14] Shibuya S, Tatsuoka F, Teachavorasinskun S, Kong XJ, Abe F, Kim YS, et al. Elastic deformation properties of geomaterials. Soils Found 1992;32:26–46.
[15] Poorooshasb HB, Holubec I, Sherbourne AN. Yielding and flow of sand in triaxial compression: Parts II and III. Can Geotech J 1967;4:376–97. http://dx.doi.org/10.1139/t67-066.
[16] Tatsuoka F, Ishihara K. Yielding of sand in triaxial compression. SOILS Found 1974;14:63–76. http://dx.doi.org/10.3208/sandf1972.14.2_63.
[17] Ishihara K, Tatsuoka F, Yasuda S. Undrained deformation and liquefaction of sand under cyclic stresses. SOILS Found 1975;15:29–44. http://dx.doi.org/10.3208/sandf1972.15.29.
[18] Vermeer PA. A double hardening model for sand. Géotechnique 1978;28:413–33. http://dx.doi.org/10.1680/geot.1978.28.4.413.
[19] Lade PV. Elasto-plastic stress-strain theory for cohesionless soil with curved yield surfaces. Int J Solids Struct 1977;13:1019–35. http://dx.doi.org/10.1016/0020-7683(77)90073-7.
[20] Miura N, Murata H, Yasufuku N. Stress-strain characteristics of sand in a particle-crushing region. SOILS Found 1984;24:77–89. http://dx.doi.org/10.3208/sandf1972.24.77.
[21] Kuwano R, Jardine RJ. A triaxial investigation of kinematic yielding in sand. Géotechnique 2007;57:563–79. http://dx.doi.org/10.1680/geot.2007.57.7.563.
[22] Jardine RJ. Some observations on the kinematic nature of soil stiffness. Soils Found 1992;32:111–24. http://dx.doi.org/10.3208/sandf1972.32.2_111.
[23] Malandraki V, Toll DG. The definition of yield for bonded materials. Geotech Geol Eng 1996;14:67–82. http://dx.doi.org/10.1007/BF00431235.
[24] Mroz Z. On the description of anisotropic workhardening. J Mech Phys Solids 1967;15:163–75.
[25] Tavenas F, Des Rosiers J-P, Leroueil S, La Rochelle P, Roy M. The use of strain energy as a yield and creep criterion for lightly overconsolidated clays. Géotechnique 1979;29:285–303. http://dx.doi.org/10.1680/geot.1979.29.3.285.
[26] Graham J, Noonan ML, Lew KV. Yield states and stress–strain relationships in a natural plastic clay. Can Geotech J 1983;20:502–16. http://dx.doi.org/10.1139/t83-058.
[27] Jovičić V, Coop MR. Stiffness of coarse-grained soils at small strains. Géotechnique 1997;47:545–61. http://dx.doi.org/10.1680/geot.1997.47.3.545.
[28] Magnanimo V, La Ragione L, Jenkins JT, Wang P, Makse HA. Characterizing the shear and bulk moduli of an idealized granular material. EPL Europhysics Lett 2008;81:34006. http://dx.doi.org/10.1209/0295-5075/81/34006.
[29] Goddard JD. Nonlinear elasticity and pressure-dependent wave speeds in granular media. Proc R Soc A Math Phys Eng Sci 1990;430:105–31. http://dx.doi.org/10.1098/rspa.1990.0083.

[30] de Bono JP, McDowell GR. The fractal micro mechanics of normal compression. Comput Geotech 2016;78:11–24. http://dx.doi.org/10.1016/j.compgeo.2016.04.018.
[31] McDowell GR, Daniell CM. Fractal compression of soil. Géotechnique 2001;51:173–6. http://dx.doi.org/10.1680/geot.2001.51.2.173.
[32] Borkovec M, De Paris W, Peikert R. The fractal dimension of the apollonian sphere packing. Fractals 1994;2:521–6. http://dx.doi.org/10.1142/S0218348X94000739.
[33] Palmer AC, Sanderson TJO. Fractal crushing of ice and brittle solids. Proc R Soc A Math Phys Eng Sci 1991;433:469–77. http://dx.doi.org/10.1098/rspa.1991.0060.
[34] Turcotte DL. Fractals and fragmentation. J Geophys Res 1986;91:1921. http://dx.doi.org/10.1029/JB091iB02p01921.
[35] Atkinson JH, Richardson D, Stallebrass SE. Effect of recent stress history on the stiffness of overconsolidated soil. Géotechnique 1990;40:531–40. http://dx.doi.org/10.1680/geot.1990.40.4.531.